

## THE RELATIONSHIP BETWEEN BLACK HOLE GROWTH AND STAR FORMATION IN SEYFERT GALAXIES

ALEKSANDAR M. DIAMOND-STANIC<sup>1,2</sup>, GEORGE H. RIEKE<sup>3</sup>

*Accepted for publication in ApJ*

### ABSTRACT

We present estimates of black hole accretion rates and nuclear, extended, and total star-formation rates for a complete sample of Seyfert galaxies. Using data from the Spitzer Space Telescope, we measure the active galactic nucleus (AGN) luminosity using the [O IV]  $\lambda 25.89 \mu\text{m}$  emission line and the star-forming luminosity using the  $11.3 \mu\text{m}$  aromatic feature and extended  $24 \mu\text{m}$  continuum emission. We find that black hole growth is strongly correlated with nuclear ( $r < 1 \text{ kpc}$ ) star formation, but only weakly correlated with extended ( $r > 1 \text{ kpc}$ ) star formation in the host galaxy. In particular, the nuclear star-formation rate (SFR) traced by the  $11.3 \mu\text{m}$  aromatic feature follows a relationship with the black hole accretion rate (BHAR) of the form  $SFR \propto \dot{M}_{BH}^{0.8}$ , with an observed scatter of 0.5 dex. This SFR–BHAR relationship persists when additional star formation in physically matched  $r = 1 \text{ kpc}$  apertures is included, taking the form  $SFR \propto \dot{M}_{BH}^{0.6}$ . However, the relationship becomes almost indiscernible when total SFRs are considered. This suggests a physical connection between the gas on sub-kpc and sub-pc scales in local Seyfert galaxies that is not related to external processes in the host galaxy. It also suggests that the observed scaling between star formation and black hole growth for samples of AGNs will depend on whether the star formation is dominated by a nuclear or extended component. We estimate the integrated black hole and bulge growth that occurs in these galaxies and find that an AGN duty cycle of 5–10% would maintain the ratio between black hole and bulge masses seen in the local universe.

*Subject headings:* galaxies: active, galaxies: nuclei, galaxies: Seyfert

### 1. INTRODUCTION

The discovery of correlations between the masses of supermassive black holes and the properties of galaxy bulges such as mass (Kormendy & Richstone 1995; Magorrian et al. 1998; Marconi & Hunt 2003; Häring & Rix 2004) and velocity dispersion (Ferrarese & Merritt 2000; Gebhardt et al. 2000; Tremaine et al. 2002) suggests a connection between the processes that regulate the growth of the central black hole and the galaxy bulge. Some models have explained this connection via energetic feedback from the accreting black hole (Silk & Rees 1998; Wyithe & Loeb 2003; Di Matteo et al. 2005; Somerville et al. 2008), which is often assumed to be triggered by galaxy mergers (e.g., Kauffmann & Haehnelt 2000; Hopkins et al. 2005). While such violent, merger-driven activity may be important for fueling luminous quasars, secular processes in the host galaxy (e.g., Hopkins & Hernquist 2006; Jogee 2006) may be sufficient to explain the black hole accretion rates (BHARs) of lower-luminosity active galactic nuclei (AGNs) such as Seyfert galaxies.

Important insights regarding the black hole–galaxy bulge connection and mechanisms for fueling AGNs can be obtained by studying the stellar populations of AGN host galaxies. There is evidence that circumnuclear stellar populations around AGNs include a relatively young component (e.g., Cid Fernandes et al. 2001; Davies et al. 2007; Riffel et al. 2009) and that

higher luminosity AGNs tend to be associated with younger stellar populations (e.g., Kauffmann et al. 2003; Wild et al. 2007). This connection may be driven by the fact that both black hole growth and star formation occur when large amounts of gas are injected into the central region of a galaxy (e.g., Sanders et al. 1988; Barnes & Hernquist 1991; Storch-Bergmann et al. 2001), although a mechanism is necessary to transport gas from  $r \sim 100 \text{ pc}$  down to sub-pc scales, regardless of the external fuel supply (e.g., Shlosman et al. 1990; Wada 2004; Escala 2007; Hopkins & Quataert 2010). A more direct connection between nuclear star formation and AGN activity has also been proposed where mass loss from evolved stars (e.g., Norman & Scoville 1988; Ciotti & Ostriker 2007) or angular-momentum loss associated with supernova-generated turbulence (e.g., von Linden et al. 1993; Hobbs et al. 2011) supplies the necessary material to the black hole accretion disk.

Measurements of ongoing star formation in AGN host galaxies are useful for constraining the above models, but standard star-formation rate (SFR) diagnostics such as the ultraviolet (UV) continuum, the H $\alpha$  emission line, or the infrared (IR) continuum (e.g., Kennicutt 1998a) are often contaminated by the AGN itself. The mid-IR aromatic (also known as PAH) features offer a solution because they probe the strength of the UV radiation field in photo-dissociation regions near young, massive stars (e.g., Peeters et al. 2004; Tielens 2005; Smith et al. 2007a). While high-energy photons or shocks associated with the AGN could destroy the molecular carriers of the aromatic features (e.g., Voit 1992; Genzel et al. 1998), Diamond-Stanic & Rieke (2010) showed that the  $11.3 \mu\text{m}$  feature remains a valid measure of the SFR for

<sup>1</sup> Center for Astrophysics and Space Sciences, University of California, San Diego, La Jolla, CA, 92093

<sup>2</sup> Center for Galaxy Evolution Fellow

<sup>3</sup> Steward Observatory, University of Arizona, Tucson, AZ, 85721

the nuclear environments of local Seyfert galaxies.

Previous studies that have used the aromatic features to assess the level of star formation in AGN host galaxies have found it to be correlated with the AGN luminosity (e.g., Imanishi & Wada 2004; Schweitzer et al. 2006; Shi et al. 2007; Netzer et al. 2007; Lutz et al. 2008; Shi et al. 2009). This is broadly consistent with models where star formation and AGN activity are both triggered by an external supply of cold gas or models where nuclear star formation fuels subsequent AGN activity. However, it is unclear how this empirical relationship behaves for a more complete sample of AGNs, how it varies as function of scale in the galaxy (e.g., nuclear v. extended star formation), or to what extent there are differences as a function of AGN luminosity or obscuration (e.g., Lutz et al. 2010).

In this paper, we extend the study of SFRs in AGN host galaxies to a complete sample of Seyfert galaxies drawn from the revised Shapley–Ames galaxy catalog (RSA, Sandage & Tammann 1987; Maiolino & Rieke 1995; Ho et al. 1997a). All galaxies have nuclear mid-IR spectra from the Infrared Spectrograph (IRS, Houck et al. 2004) and imaging from the Multiband Imaging Photometer for Spitzer (MIPS, Rieke et al. 2004) onboard the Spitzer Space Telescope (Werner et al. 2004), and we are able to treat nuclear ( $< 1$  kpc) and extended regions separately. This spatially resolved information allows us to assess the extent to which star formation and black hole accretion activity are physically connected. We present measurements of BHARs based on the [O IV]  $\lambda 25.89 \mu\text{m}$  emission line (e.g., Diamond-Stanic et al. 2009; Rigby et al. 2009), nuclear SFRs based on the  $11.3 \mu\text{m}$  aromatic feature (e.g., Diamond-Stanic & Rieke 2010), and extended SFRs based on  $24 \mu\text{m}$  flux (e.g., Rieke et al. 2009). We explore the relationships among these quantities and the constraints they place on models of black hole growth and galaxy evolution.

## 2. SAMPLE, DATA, AND MEASUREMENTS

We consider the RSA Seyfert sample analyzed by Diamond-Stanic et al. (2009), which includes the 89 Seyferts brighter than  $B_T = 13$  from Maiolino & Rieke (1995) and Ho et al. (1997a). This galaxy-magnitude-limited sample is unique in its sensitivity to low-luminosity and highly obscured AGNs (Maiolino & Rieke 1995; Ho et al. 1997a). The median distance of the sample is 22 Mpc, where the  $3.7''$  slit width of the IRS Short-Low (SL) module subtends 390 pc. Distances and Seyfert types are compiled by Diamond-Stanic et al. (2009).

For the analysis of BHARs, we use [O IV]  $\lambda 25.89 \mu\text{m}$  emission-line fluxes from Pereira-Santaella et al. (2010), which are based on data from the Long-High IRS module. For the nine galaxies without [O IV] measurements from Pereira-Santaella et al. (2010), we use [O IV] upper limits Diamond-Stanic et al. (2009), which are based on data from the Long-Low IRS module. When considering [O IV]/[Ne II] ratios, we use [Ne II] fluxes from Pereira-Santaella et al. (2010), which are based on data from the Short-High IRS module. Among the 84 sources with  $11.3 \mu\text{m}$  aromatic feature measurements (see below), we focus our analysis on the 74 galaxies with [O IV]/[Ne II]  $> 0.15$ , including 12 sources with [O IV] upper limits that are consistent with this ratio. For these

galaxies the contribution of star formation to [O IV] is sub-dominant ( $< 30\%$ , Pereira-Santaella et al. 2010), so we are able to use their [O IV] fluxes to robustly estimate BHARs.

For the analysis of nuclear SFRs (Section 4), we use measurements of the  $11.3 \mu\text{m}$  aromatic feature and the [Ne II]  $\lambda 12.81 \mu\text{m}$  emission line based on data from the IRS SL module. We used the IRS SL module (rather than the SH module) for [Ne II] SFRs to enable comparisons with aromatic-based SFRs in the same aperture. Following Diamond-Stanic & Rieke (2010), one-dimensional spectra were extracted using CUBISM (Smith et al. 2007a) with small apertures ( $3.6'' \times 7.2''$ ) designed to isolate nuclear emission, and spectral fitting was performed with PAHFIT (Smith et al. 2007b). For three sources (NGC3031, NGC3783, NGC4151), we did not obtain an adequate continuum fit near  $11.3 \mu\text{m}$ , so we defined the local continuum using a power-law fit in the  $\lambda = 10.75\text{--}10.9 \mu\text{m}$  and  $\lambda = 11.65\text{--}11.85 \mu\text{m}$  regions. Our measurements are compiled in Table 1. We exclude two sources (CIRCINUS, NGC1068) with saturated SL2 data and three sources (NGC777, NGC4168, NGC4472) without  $11.3 \mu\text{m}$  aromatic feature or [O IV]  $\lambda 25.89 \mu\text{m}$  detections, leaving a sample of 84 galaxies.

Aperture corrections are necessary to determine total nuclear fluxes because the above measurements only cover the central portion ( $1.2 \times 2.3 \lambda/D$ ) of the point-spread function (PSF) at  $\lambda \approx 12 \mu\text{m}$ . Using the IRAC channel 4 ( $8.0 \mu\text{m}$ ) PSF, scaled to match the expected beam size at  $\lambda = 11.3 \mu\text{m}$  ( $\lambda = 12.8 \mu\text{m}$ ), we find that our extraction aperture contains only 51.9% (45.3%) of the total flux from a point source. When determining SFRs, we therefore apply an aperture correction of 1.93 (2.21) to the  $11.3 \mu\text{m}$  aromatic feature ([Ne II]) fluxes.

Using MIPS  $24 \mu\text{m}$  images, we also consider the star formation in regions of each galaxy that are outside the IRS SL  $3.6'' \times 7.2''$  extraction aperture. We measure  $24 \mu\text{m}$  fluxes in circular apertures with radii  $r = 2.9''$ ,  $r = 1$  kpc, and  $r = r_{\text{galaxy}}$ . For each galaxy we attribute all the  $24 \mu\text{m}$  flux measured in the  $2.9''$  aperture (diameter  $\approx \lambda/D$ )<sup>4</sup> to a central point source (i.e., unresolved emission from both the AGN and nuclear star formation) and we use aperture corrections based on the MIPS  $24 \mu\text{m}$  PSF to determine the point-source contribution in the larger apertures. We exclude these contributions and convert the remaining fluxes into SFRs using the Rieke et al. (2009) calibration. The choice of  $r = 1$  kpc matches the area subtended by the  $3.6'' \times 7.2''$  aperture for the most distant galaxies and corresponds to the smallest physical aperture that can be used for the whole sample<sup>5</sup>.

## 3. BLACK HOLE ACCRETION RATES

The [O IV] line has been shown to be an accurate tracer of AGN intrinsic luminosity (Meléndez et al. 2008a; Rigby et al. 2009; Diamond-Stanic et al. 2009). The line is dominated by the AGN unless the IR luminosity associated with SF exceeds the AGN intrinsic luminosity by an order of magnitude (Pereira-Santaella et al.

<sup>4</sup>  $r = (3.6'' \times 7.2''/\pi)^{0.5} = 2.9''$

<sup>5</sup>  $r = 2.9''$  corresponds to  $r = 0.97$  kpc at  $D = 70$  Mpc. The only galaxy with  $D > 70$  Mpc is Mrk 509 (Diamond-Stanic et al. 2009).

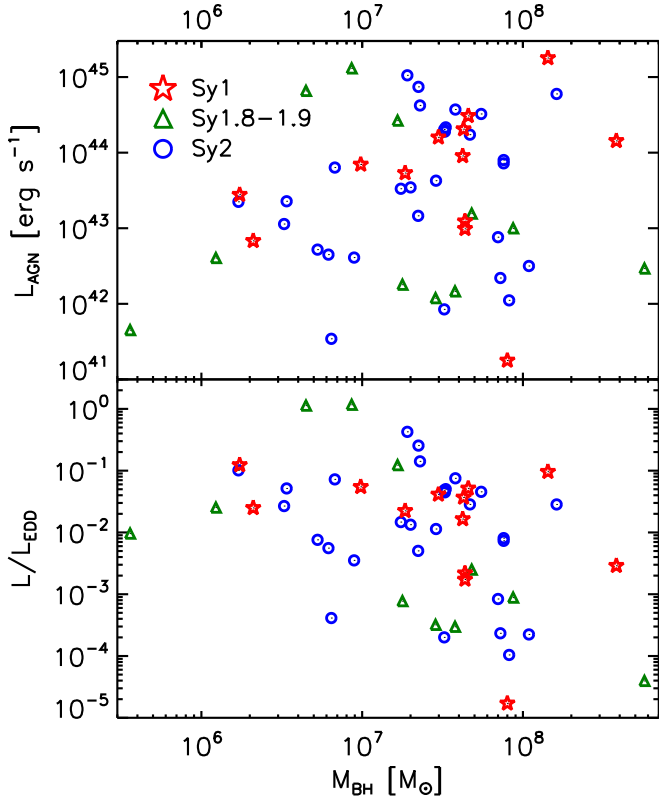


FIG. 1.— The demographics of AGN luminosity, Eddington ratio, and black hole mass for the RSA Seyfert sample. The sample includes low- to moderate-luminosity AGNs with masses generally below  $10^8 M_\odot$ . The most rapidly accreting sources with  $L/L_{\text{Edd}} > 0.1$  all have  $M_{\text{BH}} < 3 \times 10^7 M_\odot$ .

2010). We use the calibration of Rigby et al. (2009) to convert between [O IV] luminosity and AGN intrinsic luminosity,  $L_{\text{AGN}} = L_{[\text{O IV}]} \times 2550$ , which has an rms scatter of 0.4 dex. Assuming a radiative efficiency  $\eta = 0.1$  ( $L_{\text{AGN}} = \eta \dot{M}_{\text{BH}} c^2$ ), this is equivalent to the following:

$$\dot{M}_{\text{BH}} (M_\odot \text{ yr}^{-1}) = 1.7 \times 10^{-9} L([\text{O IV}], L_\odot) \quad (1)$$

We note that there are theoretical expectations that the radiative efficiency may drop at both high ( $L/L_{\text{Edd}} > 1$ , e.g., Abramowicz et al. 1988) and low ( $L/L_{\text{Edd}} < 0.01$ , e.g., Narayan & Yi 1995) accretion rates due to advection of matter onto the black hole. The latter regime is relevant for our sample, such that equation 1 may underestimate the true mass accretion rate for sources with small  $L/L_{\text{Edd}}$  values.

To assess the demographics of the sample in terms of the ratio of the AGN intrinsic luminosity to the Eddington luminosity,  $L_{\text{Edd}} = 1.3 \times 10^{46} (M_{\text{BH}}/10^8 M_\odot) \text{ erg s}^{-1}$ , we gathered estimates of black hole mass from the literature based on high-resolution gas, stellar, or maser dynamics (5 objects), reverberation mapping (10 objects), and bulge velocity dispersion (46 objects). The values of AGN intrinsic luminosity, black hole mass, and Eddington ratio for the

sample are shown in Figure 1 and compiled in Table 1. Most objects fall in the range  $L_{\text{AGN}} = 10^{42} - 10^{45} \text{ erg s}^{-1}$ ,  $M_{\text{BH}} = 10^6 - 10^8 M_\odot$ , and  $L/L_{\text{Edd}} = 10^{-4} - 1$ .

#### 4. NUCLEAR STAR-FORMATION RATES

The mid-IR aromatic features (e.g., Peeters et al. 2004; Smith et al. 2007a; Calzetti et al. 2007), the [Ne II] line (e.g., Ho & Keto 2007; Díaz-Santos et al. 2010), and the  $24 \mu\text{m}$  continuum luminosity (e.g., Calzetti et al. 2007; Rieke et al. 2009) can all be used as tracers of the SFR for normal star-forming galaxies. However, when a galaxy contains a central AGN, dust heated by the AGN will likely dominate the  $24 \mu\text{m}$  continuum (e.g., Brand et al. 2006), ionizing photons from the AGN can contribute significantly to [Ne II] (e.g., Groves et al. 2006; Pereira-Santaella et al. 2010), and high-energy photons or shocks associated with the AGN may destroy or modify the molecules that produce the mid-IR aromatic features (e.g., Voit 1992; O’Dowd et al. 2009; Diamond-Stanic & Rieke 2010). Nonetheless, Diamond-Stanic & Rieke (2010) showed that the  $11.3 \mu\text{m}$  aromatic feature is robust to the effects of AGN- and shock-processing, and Meléndez et al. (2008b) outlined a method to determine the star-formation contribution to [Ne II] for AGNs. In this section, we evaluate the merit of the  $11.3 \mu\text{m}$  aromatic feature and the [Ne II] emission line for estimating nuclear SFRs of AGN host galaxies.

##### 4.1. SFR Calibrations

We used the Rieke et al. (2009) star-forming galaxy templates to convert the  $11.3 \mu\text{m}$  aromatic feature and [Ne II] emission-line strengths into SFRs. Based on spectral decompositions with PAHFIT, we determined the strength of these features for the templates in the  $L_{\text{IR}} = 10^{9.75} - 10^{10.75} L_\odot$  range, which are appropriate for the nuclear SFRs in the sample ( $< 10 M_\odot \text{ yr}^{-1}$ ). For these templates, the  $11.3 \mu\text{m}$  aromatic feature contributes  $1.2\% \pm 0.1\%$  of the IR luminosity, while [Ne II] contributes  $0.13\% \pm 0.01\%$  (above  $L_{\text{IR}} = 10^{11} L_\odot$  these fractions drop to  $\sim 0.5\%$  and  $\sim 0.07\%$ , respectively). Using the Rieke et al. (2009) calibration between  $L_{\text{IR}}$  and SFR<sup>6</sup>, we find for this luminosity range:

$$\text{SFR}(M_\odot \text{ yr}^{-1}) = 9.6 \times 10^{-9} L(11.3 \mu\text{m}, L_\odot) \quad (2)$$

$$\text{SFR}(M_\odot \text{ yr}^{-1}) = 8.9 \times 10^{-8} L([\text{Ne II}], L_\odot) \quad (3)$$

We note that equation 2 of Ho & Keto (2007) implies that [Ne II] contributes, on average, only  $\sim 0.05\%$  of the IR luminosity (albeit with a large scatter of 0.51 dex). Such a small  $L_{[\text{Ne II}]} / L_{\text{IR}}$  ratio is more consistent with the Rieke et al. (2009) templates above  $L_{\text{IR}} = 10^{11} L_\odot$ . For lower luminosities, Treyer et al. (2010) note that the sample used by Ho & Keto (2007) includes a number of low-metallicity galaxies where [Ne III] is the dominant Ne species (e.g., Wu et al. 2006), resulting in smaller  $L_{[\text{Ne II}]} / L_{\text{IR}}$  ratios. Thus for the sources considered in this paper, our equation 3 is more appropriate for converting [Ne II] luminosities into SFRs.

<sup>6</sup> The Rieke et al. (2009) calibration yields SFRs that are 0.66 times those from the Kennicutt (1998a) calibration due to different assumptions about the stellar initial mass function.

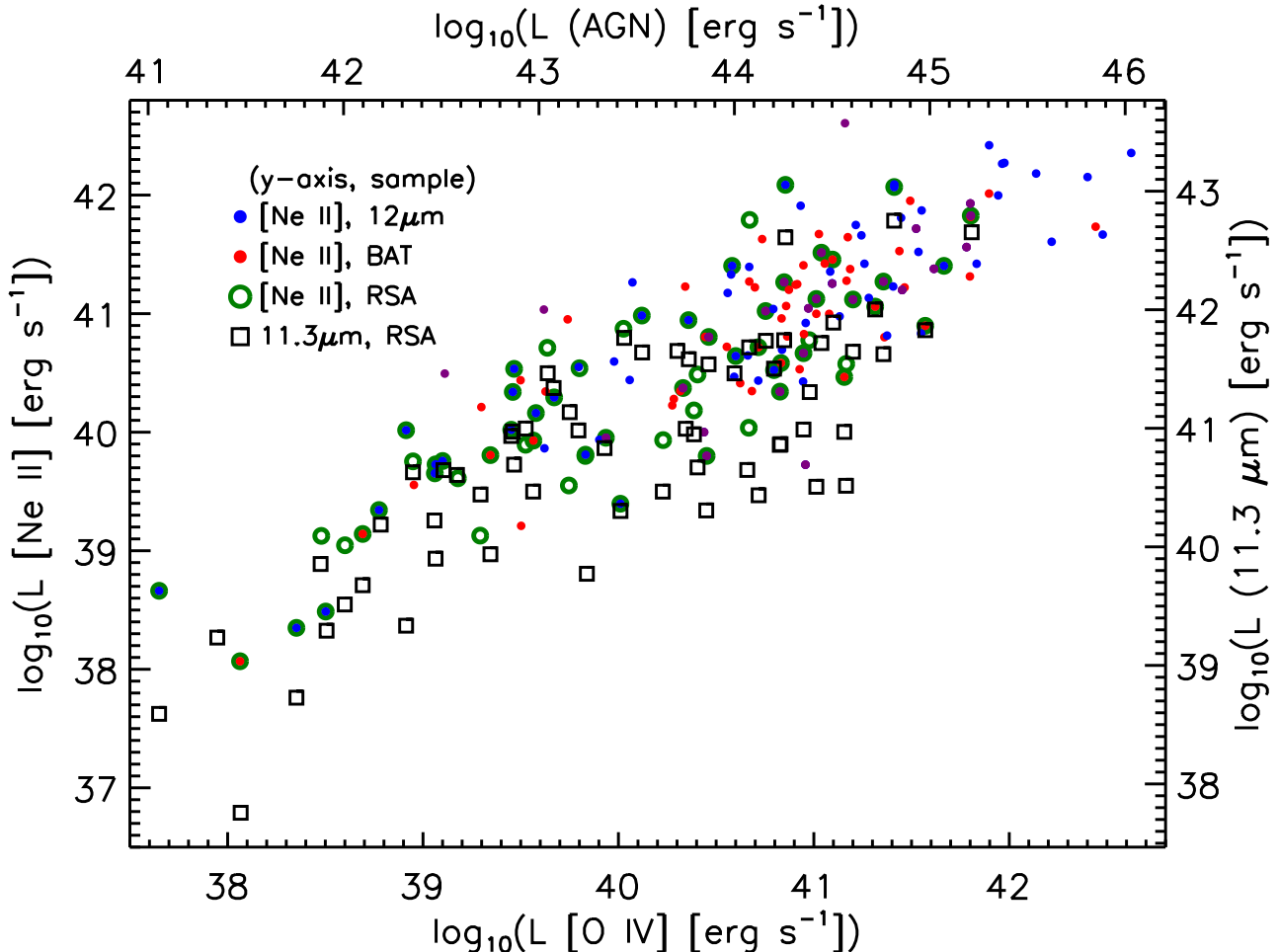


FIG. 2.— The relationship between [Ne II], 11.3  $\mu\text{m}$  aromatic feature, and [O IV] luminosity. We show the [Ne II]–[O IV] relationship for the 12 micron, Swift-BAT, and RSA samples, as well as the aromatic–[O IV] relationship for the RSA sample. The [Ne II] and aromatic-feature axes are normalized based on their typical ratio in star-forming galaxies, and the handful of starburst-dominated Seyferts with  $[\text{O IV}]/[\text{Ne II}] < 0.15$  are not plotted. This figure illustrates that [Ne II]–[O IV] relationships is tighter than the aromatic–[O IV] relationship, with the discrepancy being driven by sources with larger [Ne II]-to-aromatic-feature ratios.

#### 4.2. Comparing Aromatic and [Ne II] SFRs

We show the relationship between [Ne II], [O IV], and 11.3  $\mu\text{m}$  aromatic feature luminosities for RSA Seyferts in Figure 2. For reference, we also show the [Ne II]–[O IV] relationship for Seyferts from the 12  $\mu\text{m}$  sample (e.g., Tommasin et al. 2010) and the Swift-BAT sample (e.g., Weaver et al. 2010) that are not starburst dominated (i.e., excluding the  $\approx 10\%$  of sources with  $[\text{O IV}]/[\text{Ne II}] < 0.15$ , see Section 2). This figure illustrates that there is less scatter in the [Ne II]–[O IV] relationship (0.41 dex) than in the aromatic–[O IV] relationship (0.52 dex), implying a tighter connection between the two quantities. This figure also illustrates that if one attributes all of the [Ne II] flux to star formation, the [Ne II]-based SFR often exceeds the aromatic-based SFR.

To investigate this behavior in more detail, we compare aromatic and [Ne II] SFRs as a function of the equivalent width (EW) of the 11.3  $\mu\text{m}$  aromatic feature in the top panel of Figure 3. We find good agreement between aromatic and [Ne II] SFRs for sources with  $\text{EW}(11.3 \mu\text{m}) > 0.3 \mu\text{m}$ , with 0.2 dex of scatter around the median ra-

tio  $\text{SFR}_{[\text{Ne II}]} / \text{SFR}_{11.3 \mu\text{m}} = 1.14$ , consistent with previous results from Diamond-Stanic & Rieke (2010) for a subset of this sample. The largest outlier in this regime, NGC2639, shows evidence for suppressed aromatic features (Diamond-Stanic & Rieke 2010). However, for sources with  $\text{EW}(11.3 \mu\text{m}) < 0.3 \mu\text{m}$ , the [Ne II] SFR estimates are systematically larger than the aromatic SFRs. Given that the aromatic feature EW is a proxy for the ratio of star-forming to AGN luminosity (e.g., Genzel et al. 1998), this behavior illustrates that the SFR discrepancy is associated with AGN-dominated sources.

In the bottom panel of Figure 3, we show that the sources with discrepant SFRs also tend to have larger  $[\text{O IV}]/[\text{Ne II}]$  ratios, suggesting that the radiation field is dominated by the AGN. The typical  $[\text{O IV}]/[\text{Ne II}]$  ratio for AGNs is  $\sim 3$  (e.g., Sturm et al. 2002; Meléndez et al. 2008b; Pereira-Santaella et al. 2010), so for sources with  $[\text{O IV}]/[\text{Ne II}] > 3$  and large [Ne II]-to-aromatic-feature ratios, it is likely that the observed [Ne II] is dominated by the AGN rather than star formation. For sources

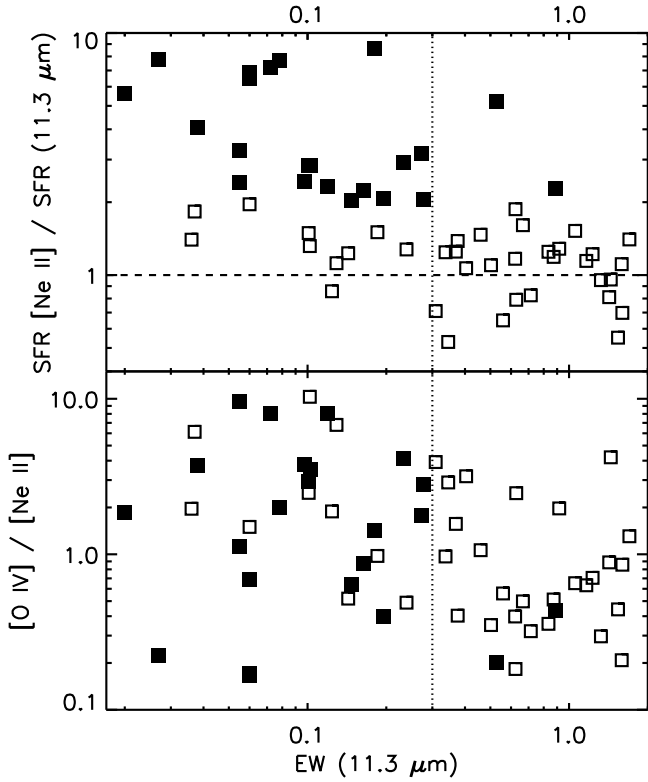


FIG. 3.— Top panel: The ratio of SFRs derived from the [Ne II] line to SFRs derived from the  $11.3\ \mu\text{m}$  aromatic feature as a function of  $\text{EW}(11.3\ \mu\text{m})$ . Sources whose [Ne II] and aromatic SFRs differ by more than a factor of two are noted by filled symbols. This ratio scatters around unity (dashed line) for sources with  $\text{EW}(11.3\ \mu\text{m}) > 0.3\ \mu\text{m}$  (dotted line). However, sources with smaller EWs tend to have systematically larger [Ne II]-to-aromatic-feature ratios. Bottom panel: The  $[\text{O IV}]/[\text{Ne II}]$  ratio as a function of  $\text{EW}(11.3\ \mu\text{m})$ . Sources with discrepant [Ne II] SFRs are most commonly found in the AGN-dominated region (top-left) of this plot. The two sources with  $[\text{O IV}]/[\text{Ne II}] < 0.3$  and  $\text{EW}(11.3\ \mu\text{m}) < 0.1\ \mu\text{m}$  (NGC3031, NGC1275) are discussed in the text.

with large [Ne II]-to-aromatic-feature ratios but smaller  $[\text{O IV}]/[\text{Ne II}]$  ratios, the situation is less clear. However, the amount of [Ne II] produced by the AGN is strongly dependent on the ionization parameter (e.g., Groves et al. 2006), and it is not uncommon for the observed  $[\text{O IV}]/[\text{Ne II}]$  ratio for AGNs to be as large as  $\sim 10$  or smaller than unity (e.g., Pereira-Santaella et al. 2010, Figure 3). The two sources with  $[\text{O IV}]/[\text{Ne II}] < 0.3$  and  $\text{EW}(11.3\ \mu\text{m}) < 0.1\ \mu\text{m}$  are the nearby spiral galaxy M81 (NGC3031) and the radio galaxy Perseus A (NGC1275)<sup>7</sup>, both of which may exhibit advection-dominated accretion flows with softer spectral energy distributions (e.g., Quataert et al. 1999; Balmaverde et al. 2008; Miller et al. 2010).

<sup>7</sup> Both of these galaxies have strong silicate emission, which decreases their  $\text{EW}(11.3\ \mu\text{m})$  values because we include silicate emission as a continuum component. For a detailed analysis of M81, see Smith et al. (2010).

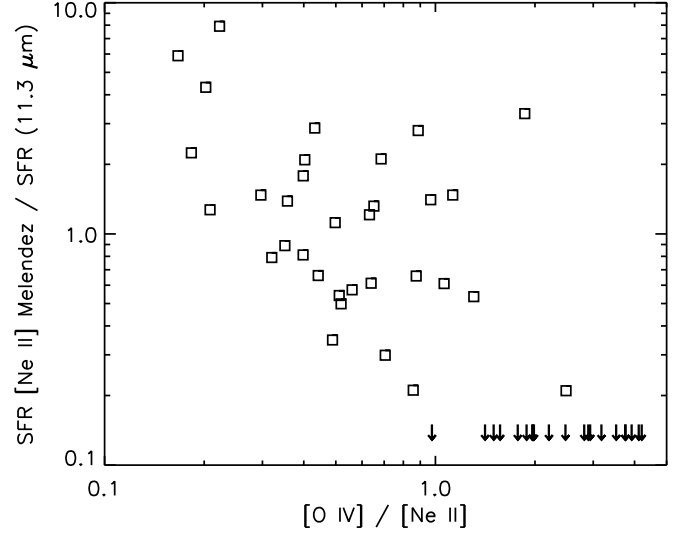


FIG. 4.— The ratio of SFRs derived from the [Ne II] line, using the method of Meléndez et al. (2008b) to subtract the AGN contribution to [Ne II], to SFRs derived from the  $11.3\ \mu\text{m}$  aromatic feature as a function of the  $[\text{O IV}]/[\text{Ne II}]$  ratio. We find that the Meléndez et al. (2008b) method can overestimate SFRs for sources with  $[\text{O IV}]/[\text{Ne II}] < 0.3$  and underestimate SFRs for sources with  $[\text{O IV}]/[\text{Ne II}] > 1$ .

Several authors have discussed the question of what fraction of [Ne II] emission is produced by the AGN (e.g., Sturm et al. 2002; Schweitzer et al. 2006; Meléndez et al. 2008b; Weaver et al. 2010; Pereira-Santaella et al. 2010). This fraction can be estimated by assuming a fiducial relationship between  $[\text{O IV}]$  and [Ne II] emission for pure AGNs (i.e., with no star formation contribution to [Ne II]), and then attributing excess [Ne II] emission to star formation. For example, (Sturm et al. 2002) adopted the ratio  $[\text{O IV}]/[\text{Ne II}] = 2.7$  for pure AGNs, and Meléndez et al. (2008b) determined a luminosity-dependent relationship between [Ne II] and  $[\text{O IV}]$  for Seyfert galaxies with undetected aromatic features, yielding a pure AGN ratio of  $[\text{O IV}]/[\text{Ne II}] = 0.9$  for sources with  $L_{[\text{O IV}]} = 10^{39}\ \text{erg s}^{-1}$  and  $[\text{O IV}]/[\text{Ne II}] = 3.1$  for sources with  $L_{[\text{O IV}]} = 10^{42}\ \text{erg s}^{-1}$ . We compare aromatic SFRs to [Ne II] SFRs estimated based on this latter method in Figure 4. There is rough agreement in the median SFR between the two methods, but there is significant disagreement on a source-by-source basis. In particular, the Meléndez et al. (2008b) method assigns  $\text{SFR}=0$  for a large number of RSA Seyferts with clearly detected aromatic features, and it gives larger SFRs for a number of sources with smaller  $[\text{O IV}]/[\text{Ne II}]$  ratios (e.g., NGC3031 and NGC1275, as discussed above).

Thus, for any individual Seyfert galaxy, it is not straightforward to determine an accurate SFR based on its [Ne II] emission line, primarily because the AGN contribution to [Ne II] varies significantly from source to source (e.g., Groves et al. 2006; Pereira-Santaella et al. 2010). If one assumed that all of the [Ne II] emission were produced by star formation, one would overestimate SFRs for AGN-dominated sources and underestimate the scatter in the relationship between AGN and

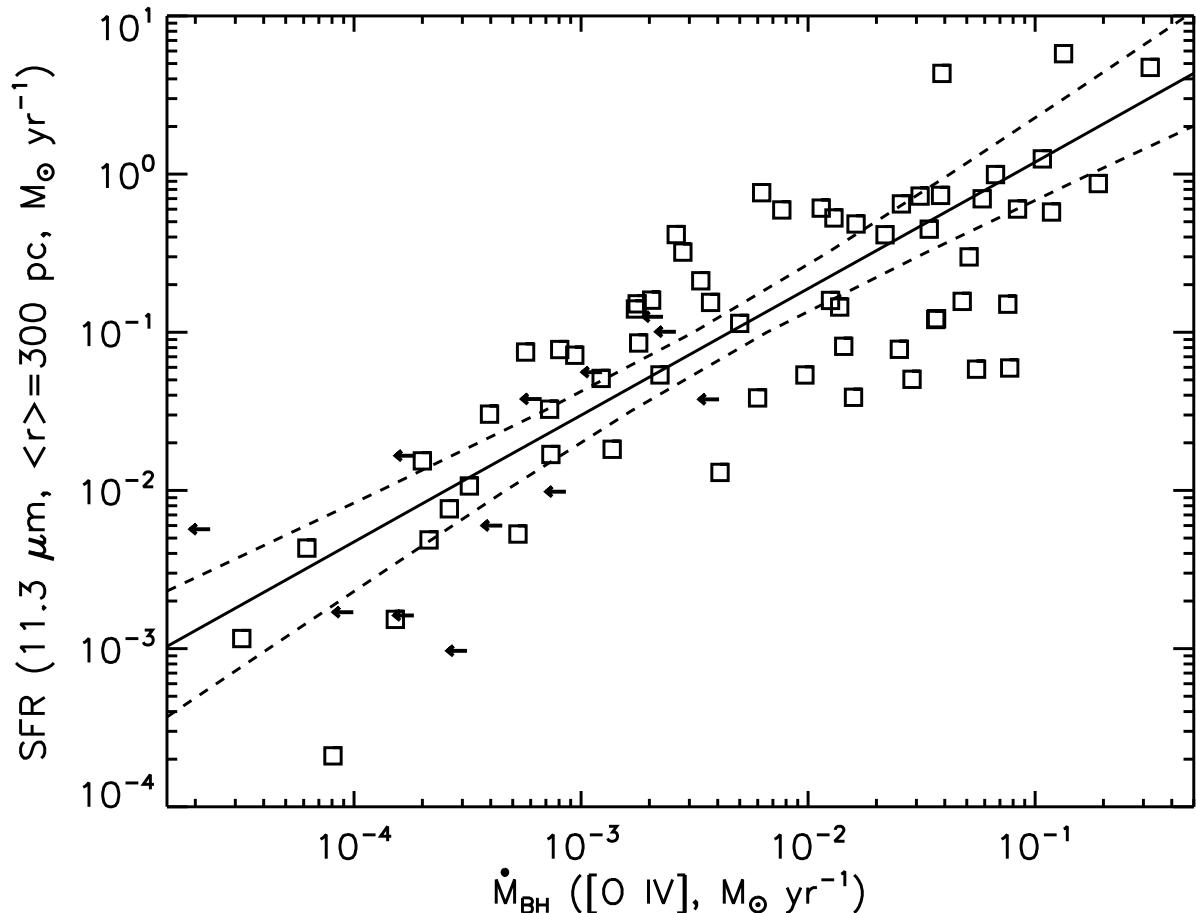


FIG. 5.— The relationship between nuclear SFR as traced by the 11.3  $\mu\text{m}$  aromatic feature and BHAR as traced by [O IV]. Seyferts with high accretion rates also tend to have enhanced nuclear SFRs. The solid line is the best-fit relationship (equation 4), and the dotted lines show the 95% confidence interval on the regression line.

star-forming luminosity (e.g., see Figure 2), thus concluding that this relationship is stronger than it actually is. The destruction of aromatic molecules by the AGN does not appear to have a significant effect on the 11.3  $\mu\text{m}$  aromatic feature in the circumnuclear environment of local Seyfert galaxies (Diamond-Stanic & Rieke 2010). That said, if such destruction were important, it would mean that the connection between star-formation rate and black hole accretion rate (a central result of this paper, see Section 5) is actually stronger than we’ve presented. We therefore adopt the 11.3  $\mu\text{m}$  aromatic feature as the most robust tracer of the SFR for our sample. We adopt an uncertainty of 0.2 dex on conversions between the 11.3  $\mu\text{m}$  aromatic feature strength and IR luminosity based on the scatter in this ratio for the SINGS sample (Smith et al. 2007a) and an additional uncertainty of 0.2 dex for conversions between IR luminosity and SFR (Rieke et al. 2009). Adding these in quadrature, the uncertainty on SFRs obtained from equation 2 is 0.28 dex.

## 5. RESULTS

### 5.1. Black Hole Accretion v. Nuclear Star Formation

In Figure 5, we show the relationship between BHAR, as traced by [O IV], and nuclear SFR, as traced by the 11.3  $\mu\text{m}$  aromatic feature. A strong correlation is apparent: Seyferts with larger BHARs tend to have larger nuclear SFRs. We use the linear regression method<sup>8</sup> outlined by Kelly (2007) to quantify the relationship between nuclear SFR and BHAR:

$$SFR(11.3 \mu\text{m}, M_{\odot} \text{ yr}^{-1}) = 7.6_{-3.9}^{+9.8} \left( \frac{\dot{M}_{BH}}{M_{\odot} \text{ yr}^{-1}} \right)^{0.80_{-0.12}^{+0.14}} \quad (4)$$

The uncertainties on the regression parameters above correspond to the interval that includes 90% of the posterior distribution for each parameter (see Table 2). The best-fit regression line and 95% confidence interval, given the uncertainties in the regression parameters, are shown as solid and dashed lines in Figure 5. The observed scatter around this relationship is 0.52 dex (treating BHAR upper limits as detections), although the posterior median estimate of the intrinsic scatter is 0.37 dex (see Ta-

<sup>8</sup> code available from the IDL Astronomy User’s Library (linmix\_err.pro), <http://idlastro.gsfc.nasa.gov/>

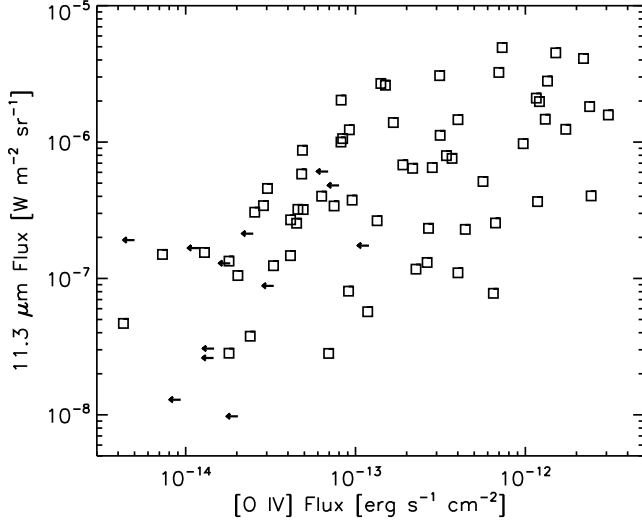


FIG. 6.— The relationship between [O IV] flux and 11.3  $\mu\text{m}$  aromatic feature flux. The correlation between these two observed quantities is statistically significant, illustrating that the connection between the derived physical quantities (nuclear SFR and BHAR) is real and not just driven by the distance-squared factor in luminosity–luminosity plots.

ble 2), suggesting that much of the observed scatter may be driven by the measurement errors on SFR and BHAR.

To test whether the relationship between SFR and BHAR could be driven by the distance dependence inherent in luminosity–luminosity plots, in Figure 6 we show the relationship between the observed quantities, 11.3  $\mu\text{m}$  aromatic feature and [O IV] flux. The correlation in this flux–flux plot is still statistically significant (Spearman’s  $\rho=0.66$ , probability of no correlation  $p < 1 \times 10^{-6}$ ; Isobe et al. 1986; Lavalley et al. 1992), confirming the reality of this relationship.

We investigate the behavior of the SFR/BHAR ratio as a function of BHAR in Figure 7; the median ratio SFR/BHAR=23 is shown as a dotted line. A mild anti-correlation exists such that sources with large accretion rates tend to have smaller SFR/BHAR ratios (Spearman’s  $\rho=-0.48$ ,  $p = 8 \times 10^{-5}$ ). Thus, consistent with the sub-linear slope in equation 4, this indicates that the nuclear SFR does not keep pace with the BHAR towards high AGN luminosities. We find no significant difference in the nuclear SFRs or SFR/BHAR ratios between different Seyfert types (see Section 6.4).

#### 5.1.1. Nuclear Star Formation in Physically Matched Apertures

As described in Section 2, we also measured 24  $\mu\text{m}$  fluxes inside  $r = 1$  kpc apertures to assess contributions from star formation that falls outside our IRS extraction aperture. In Figure 8, we show that this contribution can be significant for sources with  $D < 30$  Mpc. Since the nearby sources tend to be have smaller BHARs, including this additional star-formation contribution leads to a shallower relationship between nuclear SFR and BHAR. We show this relationship in Figure 9, which is described

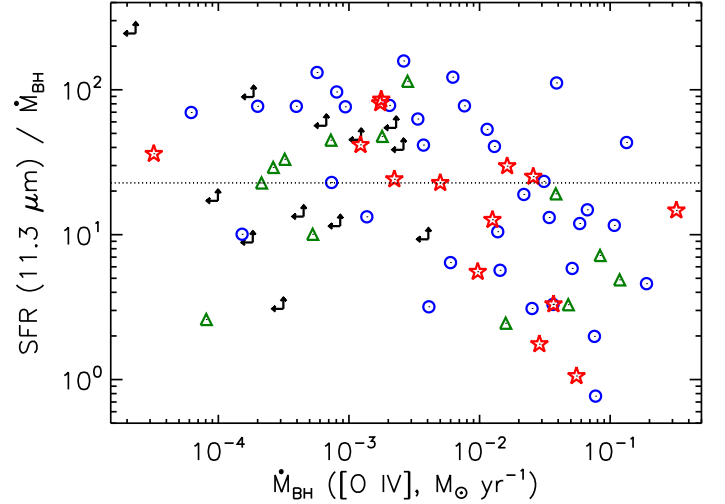


FIG. 7.— The nuclear SFR/BHAR ratio as a function of BHAR. The median ratio SFR/BHAR=23 is shown as a dotted line. There is mild anti-correlation such that sources with large accretion rates tend to have smaller SFR/BHAR ratios. Plot symbols are the same as in Figure 1.

by the following:

$$SFR(r = 1 \text{ kpc}, M_{\odot} \text{ yr}^{-1}) = 4.7^{+6.8}_{-2.3} \left( \frac{\dot{M}_{BH}}{M_{\odot} \text{ yr}^{-1}} \right)^{0.61^{+0.15}_{-0.11}} \quad (5)$$

Again, the uncertainties on the values above correspond to the interval that includes 90% of the posterior distribution for each parameter (see Table 2). The observed scatter around this relationship is 0.50 dex and the posterior median estimate of the intrinsic scatter is 0.41 dex. The bottom panel of Figure 9 illustrates how the SFR/BHAR ratio tends to decrease as a function of BHAR.

It is worth noting that our sample does not include galaxies with larger SFR/BHAR ratios by definition since this is a sample of AGNs and is limited to sources that have  $[\text{O IV}]/[\text{Ne II}] > 0.15$ , where we can accurately estimate AGN luminosities (see Section 2). Based on equations 1 and 3, this cut corresponds to a SFR/BHAR ratio of  $\approx 350$ , which is similar to the maximum ratio in Figure 9.

#### 5.2. Black Hole Accretion v. Extended Star Formation

The connection described above between black hole accretion and nuclear star formation motivates us to consider whether such a relationship also exists between black hole activity and star formation on larger scales in the host galaxy. We examine this relationship using extended ( $r > 1$  kpc) SFRs estimated from MIPS 24  $\mu\text{m}$  fluxes (see Section 2, Table 1, and Figure 10) and total SFRs estimated from the nuclear and extended components (see Figure 11).

There are correlations present in Figures 10–11, but the scatter is significantly larger than for nuclear SFRs (Figures 5 and 9). The posterior median estimate of the intrinsic scatter in the SFR–BHAR relationship is



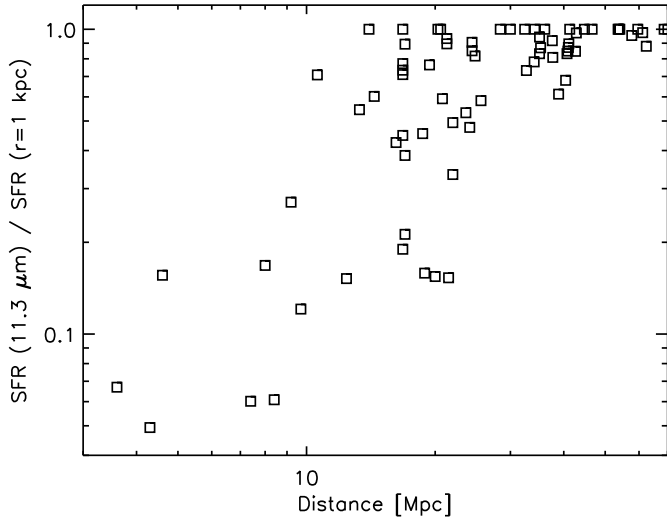


FIG. 8.— The ratio of the the SFR determined from the  $11.3\ \mu\text{m}$  feature to the SFR in a  $r = 1\ \text{kpc}$  aperture, where additional contributions from  $24\ \mu\text{m}$  emission outside the spectroscopic aperture are included, as a function of galaxy distance. Such contributions are often significant for sources with  $D < 30\ \text{Mpc}$ .

0.73 dex for  $r > 1\ \text{kpc}$  SFRs and 0.86 dex for total SFRs. Furthermore, the correlation probabilities for the flux-flux versions of these extended and total SFR relationships are not highly significant (see Table 2), illustrating that the connection between the physical quantities is weak. In addition, the observed significance is enhanced by a Malmquist-type bias against more distant galaxies with lower SFRs, related to the galaxy apparent magnitude limit of the RSA Seyfert sample.

To illustrate the stronger correlation and smaller scatter associated with nuclear SFRs, in Figure 12 we show the posterior distributions for the correlation coefficient and intrinsic scatter of the SFR–BHAR relationship when considering (1)  $11.3\ \mu\text{m}$  aromatic feature, (2)  $r = 1\ \text{kpc}$ , (3)  $r > 1\ \text{kpc}$ , and (4) total galaxy SFRs. This figure illustrates that while the BHAR correlates reasonably well with star formation on sub-kpc scales, it is only weakly related to extended and total star formation activity.

## 6. DISCUSSION

Our results present a picture where the star formation on sub-kpc scales in AGN host galaxies traces the BHAR in a somewhat sub-linear fashion, while star formation on larger scales only weakly traces the BHAR. Recently, Lutz et al. (2010) argued that host galaxy star formation only shows a clear dependence on AGN luminosity for high-luminosity sources ( $L_{\text{AGN}} > 10^{45}\ \text{erg s}^{-1}$  or  $\dot{M}_{\text{BH}} > 0.1\ \text{M}_{\odot}\ \text{yr}^{-1}$ , see their Figure 6), but our results show that this relationship persists towards lower AGN luminosities if one considers only the nuclear component of the host galaxy. Given that estimates for samples of AGNs usually provide only total SFRs (see Section 6.1), the observed scaling between SFR and BHAR may depend on whether the star formation is dominated by a nuclear or extended component.

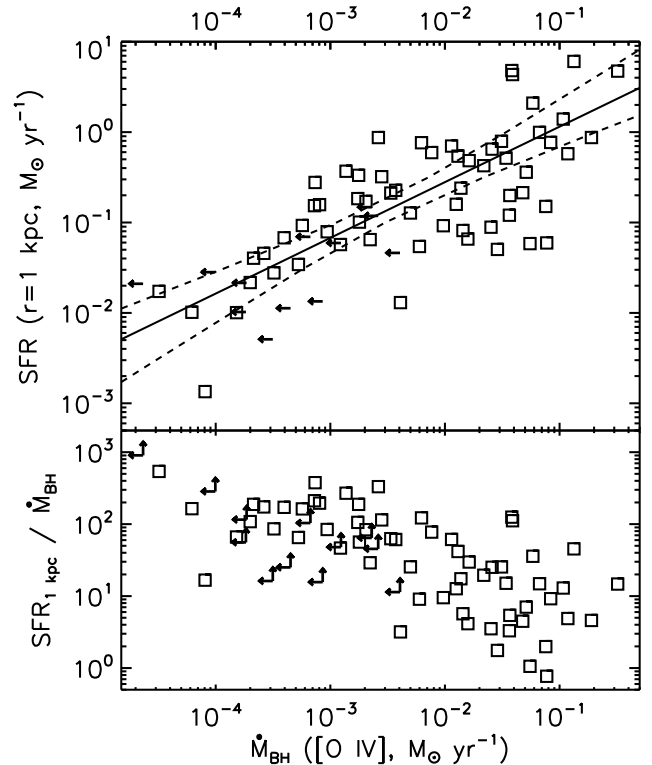


FIG. 9.— The relationship between nuclear SFR (measured on  $r = 1\ \text{kpc}$  scales) and the BHAR. A strong correlation exists, and the slope of the relationship is sub-linear as sources with larger BHARs tend to have smaller SFR/BHAR ratios (see equation 5).

### 6.1. Comparison with Previous SFR and BHAR Measurements

Several authors have estimated SFRs for AGN host galaxies and explored the relationship with BHAR. Some find an approximately linear relationship ( $\alpha \geq 0.8$ , where  $\text{SFR} \propto \dot{M}_{\text{BH}}^{\alpha}$ , e.g., Satyapal et al. 2005; Netzer 2009; Shi et al. 2009) consistent with our results for nuclear SFRs traced by the  $11.3\ \mu\text{m}$  aromatic feature (equation 4, Figure 5), while others finding a much shallower relationship ( $\alpha \leq 0.5$ , e.g., Hao et al. 2005; Silverman et al. 2009; Bonfield et al. 2011), more consistent with our results for extended and total SFRs (Figures 10–11).

Among studies that have used the aromatic features to estimate SFRs, Netzer (2009) compiled Spitzer measurements for 28  $z \sim 0.1$  QSOs (Netzer et al. 2007) and 12  $z \sim 2$  QSOs (Lutz et al. 2008) to complement their own study of a large sample of type 2 Seyferts and LINERs from the Sloan Digital Sky Survey (SDSS). The AGN luminosities for the SDSS sources were estimated using the  $[\text{O III}]\lambda 5007$  and  $[\text{O I}]\lambda 6300$  lines, and SFRs were estimated using the method of Brinchmann et al. (2004). They found a relationship of the form  $\text{SFR} \propto \dot{M}_{\text{BH}}^{0.8}$  with a SFR/BHAR ratio  $\sim 30$  for  $\dot{M}_{\text{BH}} = 0.1\ \text{M}_{\odot}\ \text{yr}^{-1}$ . Similarly, Shi et al. (2009) considered the relationship between  $5\text{--}6\ \mu\text{m}$  continuum luminosity and aromatic-feature luminosity for a sample of 89 PG quasars at



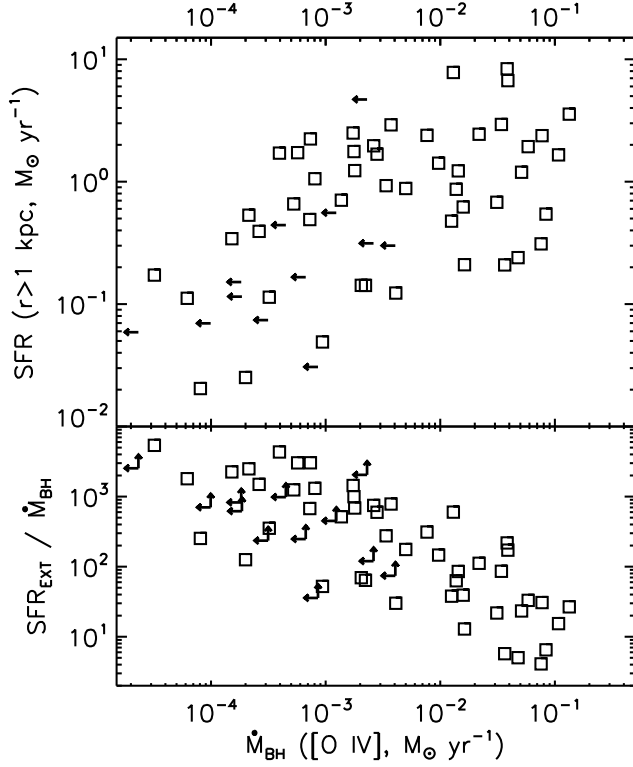


FIG. 10.— The relationship between extended SFR (measured on  $r > 1$  kpc scales) and the BHAR. Only a mild correlation exists between these quantities.

$z < 0.5$  (Shi et al. 2007) and 57 SDSS quasars at  $z \sim 1$  and found a relationship of the form  $SFR \propto \dot{M}_{BH}^{0.97 \pm 0.08}$  with a SFR/BHAR ratio  $\sim 10$  for sources with  $\dot{M}_{BH} = 1 M_{\odot} \text{ yr}^{-1}$ . These relationships are consistent with our results for aromatic-based SFRs (Section 5.1), although they extend to higher luminosities.

A number of studies have also used measurements of far-IR luminosities of AGNs to estimate host galaxy SFRs. There are uncertainties regarding poorly sampled IR spectral energy distributions and contributions from dust heated by the AGN (e.g., Schweitzer et al. 2006; Shi et al. 2007), but these estimates are nonetheless instructive. For example, Satyapal et al. (2005) expanded on the work of Dudik et al. (2005) and compiled AGN and far-IR luminosities for a sample including 86 Seyferts and quasars, for which they found a relationship of the form  $SFR \propto \dot{M}_{BH}^{0.89}$  with an SFR/BHAR ratio  $\sim 60$  at  $\dot{M}_{BH} = 0.1 M_{\odot} \text{ yr}^{-1}$ . This is similar to our Equation 4, but with a somewhat higher SFR normalization. On the other hand, a shallower relationship ( $\alpha = 0.29$ ) with a much larger SFR normalization (SFR/BHAR  $\sim 3000$  at  $\dot{M}_{BH} = 0.1 M_{\odot} \text{ yr}^{-1}$ ) was found by Hao et al. (2005) for a sample of 31 AGN-ULIRGs at  $z < 0.5$ , where excess emission at  $60 \mu\text{m}$  was attributed to star formation. More recently, such a shallow slope ( $\alpha \leq 0.5$ ) has also been found by several studies of optically selected quasars (e.g., Serjeant & Hatziminaoglou

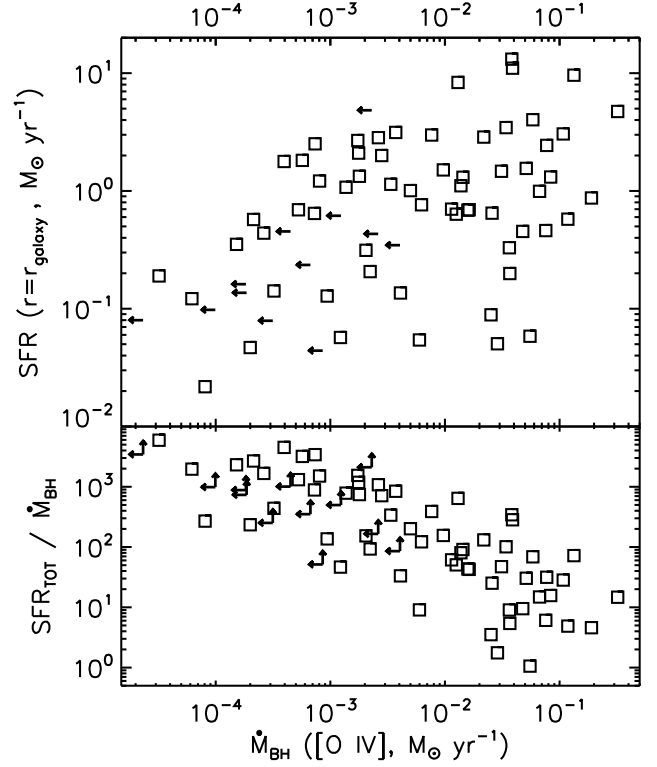


FIG. 11.— The relationship between a galaxy's total SFR and BHAR, which exhibits only a weak correlation.

2009; Hatziminaoglou et al. 2010; Bonfield et al. 2011) in fields that have Spitzer or Herschel (Pilbratt et al. 2010) coverage.

Several studies of X-ray selected AGNs have also found a shallow SFR–BHAR relationship. Silverman et al. (2009) used the  $[\text{O II}]\lambda 3727$  line to estimate SFRs for a sample of COSMOS (Scoville et al. 2007) X-ray AGNs and found  $SFR \propto \dot{M}_{BH}^{0.28 \pm 0.22}$  with a SFR/BHAR ratio  $\sim 50$  at  $\dot{M}_{BH} = 0.1 M_{\odot} \text{ yr}^{-1}$ . Atlee et al. (2011) considered a sample of X-ray and IR-selected AGNs in galaxy clusters, with SFRs estimated from spectral decompositions of mid-IR data (Assef et al. 2010), and found  $SFR \propto \dot{M}_{BH}^{0.46 \pm 0.06}$ . While these sources reside in denser environments, their AGN luminosities and total SFRs fall in the range of RSA Seyferts. Lutz et al. (2010) and Shao et al. (2010) measured  $870 \mu\text{m}$  and  $100\text{--}160 \mu\text{m}$  emission, respectively, for samples of Chandra X-ray-selected AGNs (Alexander et al. 2003; Lehmer et al. 2005; Tozzi et al. 2006), and compiled  $60 \mu\text{m}$  measurements for local AGNs detected by Swift-BAT (Cusumano et al. 2010). They also find a shallow SFR–BHAR slope ( $\alpha \sim 0.4$ ), but argue that star formation and black hole growth are more closely linked at higher AGN luminosities. Recently, Mullaney et al. (2011) found no correlation between X-ray luminosity and far-IR luminosity for moderate luminosity X-ray sources ( $L_X = 10^{42}\text{--}10^{44} \text{ erg s}^{-1}$ ) up to  $z \approx 3$ , consistent with the weak relationship we find for

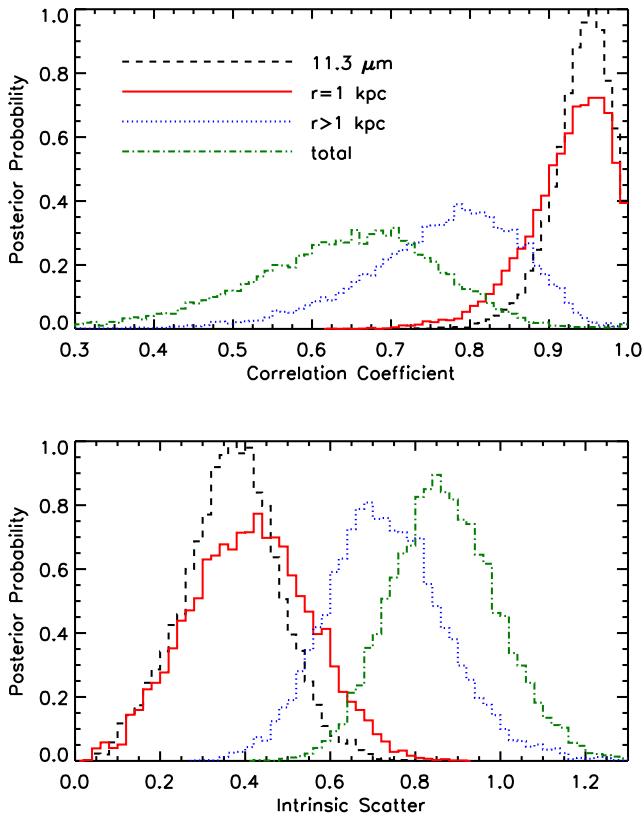


FIG. 12.— The posterior distributions for the correlation coefficient and intrinsic scatter in the SFR–BHAR relationships for different SFR values. This figure illustrates that the relationships with nuclear SFR exhibit a stronger correlation with smaller scatter than the relationships with extended and total star formation.

total SFRs.

### 6.2. Comparison with Model Predictions

A number of authors have made theoretical predictions for the behavior of the SFR and the BHAR during the AGN phase. These models differ primarily in their predictions for the nuclear SFR/BHAR ratio, ranging from  $\sim 1$  (e.g., Kawakatu & Wada 2008) to  $\sim 10^3$  (e.g., Thompson et al. 2005) for AGNs with  $\dot{M}_{BH} \sim 0.1 \text{ M}_{\odot} \text{ yr}^{-1}$ .

For example, in the galaxy merger models of Di Matteo et al. (2005) that produce a final black hole mass  $\sim 4 \times 10^7 \text{ M}_{\odot}$ , which is appropriate for our sample (see Figure 1), the SFR/BHAR ratio reaches  $\sim 200$  at the peak of star-formation activity as the galaxies coalesce and drops to  $\sim 5$  at the end of the bright AGN phase ( $\dot{M}_{BH} > 0.1 \text{ M}_{\odot} \text{ yr}^{-1}$ ). Although the RSA Seyferts show little evidence for merger activity, our results for nuclear SFRs are broadly consistent with these values. For lower accretion rates ( $\dot{M}_{BH} = 10^{-3}\text{--}10^{-2} \text{ M}_{\odot} \text{ yr}^{-1}$ ) characteristic of earlier merger phases in the Di Matteo et al. (2005) model, the SFR/BHAR ratio falls in the 500–1000 range, consistent with our results for total SFRs (see Figure 11).

The starburst disk models of Thompson et al. (2005)

that produce  $\dot{M}_{BH} \sim 0.1 \text{ M}_{\odot} \text{ yr}^{-1}$  suggest that most of the gas being supplied at an outer radius  $R_{out} = 200 \text{ pc}$  will be consumed by a starburst near that outer radius, resulting in  $\text{SFR/BHAR} \sim 10^3$ . While inconsistent with our measurements for local Seyfert galaxies, this model is perhaps consistent with the findings of Hao et al. (2005) for AGN-ULIRGs. Ballantyne (2008) used a scaled-down version of the Thompson et al. (2005) model to study less powerful starbursts around AGNs. They found  $\text{SFR/BHAR} \sim 200$  inside  $r = 100 \text{ pc}$  for a fiducial model with  $\dot{M}_{BH} \sim 0.3 \text{ M}_{\odot} \text{ yr}^{-1}$ , which is more star formation than we observe in  $r = 1 \text{ kpc}$  apertures (see Figure 9). They also predict that the SFR/BHAR ratio should increase toward lower AGN luminosities due to competition for gas between star formation and black hole accretion. This model assumes a constant gas supply, and could perhaps be reconciled with our observations if the gas supply were depleted in such a way that the SFR decreased more quickly than the BHAR.

Escala (2007) studied the evolution of the central kpc of a massive nuclear disk with a central black hole and find that the SFR and BHAR trace each other during the primary growth phase ( $\text{SFR} \propto \dot{M}_{BH}$ ) with SFR/BHAR ratios in the 3–50 range. This is consistent with our results regarding nuclear SFRs for sources with  $\dot{M}_{BH} > 0.01 \text{ M}_{\odot} \text{ yr}^{-1}$  (see Figure 9). Focusing on smaller scales, Kawakatu & Wada (2008) studied a 100 pc circumnuclear disk with accretion being driven by turbulence from supernovae. They found a correlation between SFR and BHAR only for sources with  $\dot{M}_{BH} > 0.01 \text{ M}_{\odot} \text{ yr}^{-1}$ , and they predict that the SFR/BHAR ratio should increase with AGN luminosity, reaching a maximum ratio  $\sim 2$ . This model predicts less circumnuclear star formation than we observe in  $r = 1 \text{ kpc}$  apertures, and can only be reconciled with our observations if there is  $10\times$  more star formation on  $100 \text{ pc} < r < 1 \text{ kpc}$  scales than on  $r < 100 \text{ pc}$  scales.

Hopkins & Quataert (2010) went a step further and made predictions for the relationship between SFR and BHAR as a function of radius. They used results from large-scale (100 kpc to 100 pc) simulations of galaxy mergers and barred galaxy disks, and then re-simulated the central kpc (1 kpc to 10 pc) and the central 10 pc (10 pc to 0.1 pc) at higher spatial resolution. They find SFR/BHAR ratios ranging from  $\sim 10$  for  $R < 100 \text{ pc}$  to  $\sim 30$  for  $R < 1 \text{ kpc}$ , and  $\sim 300$  for the whole galaxy, which is consistent with our results for nuclear and total SFRs. They also find  $\text{SFR} \propto \dot{M}_{BH}$  on the smallest scales ( $R < 10 \text{ pc}$ ) and  $\text{SFR} \propto \dot{M}_{BH}^{0.7}$  on larger scales, which is in general agreement with the scalings we find for nuclear star formation.

### 6.3. Implications for Black Hole and Bulge Growth

It is worthwhile to consider our measurements of nuclear SFRs and BHARs in terms of the observed scaling between galaxy bulge and black hole masses (e.g., Marconi & Hunt 2003; Häring & Rix 2004). Heckman et al. (2004) analyzed a sample of bulge-dominated galaxies from the Sloan Digital Sky Survey and found that the integrated black hole growth (from galaxies hosting AGNs) and star formation (from all galaxies) corresponded to  $\text{SFR/BHAR} \sim 10^3$ , consistent with the observed bulge/black hole mass ratio. Fu et al.

(2010) performed a similar exercise for a sample of luminous infrared galaxies and found similar results for the integrated population. For our sample, we find a median  $\text{SFR}/\text{BHAR} = 36$  on scales of  $r = 1$  kpc (the integrated total corresponds to  $\text{SFR}/\text{BHAR} = 23$ ), which is factor of  $\sim 20$  below the median bulge/black hole mass ratio (Häring & Rix 2004). This implies an AGN duty cycle of  $\sim 5\%$ , which is within a factor of two of the Seyfert fraction in the RSA galaxy sample ( $\sim 10\%$ , Ho et al. 1997a).

There are several caveats associated with the above estimate, including the fact we excluded the most star-formation dominated Seyferts (see Section 2) and that the our nuclear apertures have not been customized to match the bulge of each galaxy. A systematic bulge/disk decomposition is beyond the scope of this work, but  $r = 1$  kpc corresponds roughly to the effective radius of a  $10^{10} M_{\odot}$  bulge (Marconi & Hunt 2003; Shen et al. 2003; Graham & Worley 2008), meaning that our nuclear apertures encompass half the light of such a bulge (and less light for more massive bulges). Accounting for these effects, as well as potential bulge growth through dynamical process that relax the orbits of pre-existing stars, would tend to increase our estimate of the AGN duty cycle. We have also assumed that local Seyfert galaxies obey the black hole–bulge scaling relations defined primarily by early-type galaxies with classical bulges, which may or may not be the case (e.g., Graham 2008; Hu 2008; Greene et al. 2010; Kormendy et al. 2011).

We now consider our results in the context of AGN fueling mechanisms. A number of morphological studies of AGN host galaxies at  $z < 1$  have argued that the fueling for most systems is not merger driven (e.g., Grogin et al. 2005; Pierce et al. 2007; Gabor et al. 2009; Cisternas et al. 2011). While large-scale bars can also provide the necessary gravitational torques to drive gas down to  $\sim 100$  pc, there is not strong evidence that Seyfert galaxies exhibit a larger bar fraction than do star-forming galaxies (e.g., Ho et al. 1997b; Mulchaey & Regan 1997; Hunt & Malkan 1999). However, both Seyfert and star-forming activity appear to be associated with a higher incidence of bars than found in quiescent galaxies (Laurikainen et al. 2004; Hao et al. 2009). We have demonstrated that the BHAR is correlated with the amount of gas on sub-kpc scales (adopting the  $\text{SFR} \propto \Sigma_{\text{gas}}$  assumption of the Schmidt-Kennicutt relationship, Schmidt 1959; Kennicutt 1998b), but such gas still needs to shed most of its angular momentum to reach the black hole. Future studies with ALMA of the spatial distribution and kinematics of molecular gas down to  $\sim \text{pc}$  scales in local Seyfert galaxies will probe the nature of this fueling more directly. We note that Davies et al. (2007) and Wild et al. (2010) presented evidence for a time delay between the onset of star formation and AGN activity, which can be explained if the black hole is being fed by outflows from intermediate-age stars. Our observations are not sensitive to detecting such a  $\sim 100$  Myr time delay because the aromatic features will continue to be excited by UV photons from longer-lived B stars (e.g., Peeters et al. 2004; Díaz-Santos et al. 2010). The required loss of angular momentum could also be explained by dynamical instabilities in self-gravitating disks (e.g., Hopkins & Quataert 2010).

#### 6.4. Behavior as a Function of Seyfert Type

There have been suggestions from theoretical (e.g., Wada & Norman 2002; Ballantyne et al. 2006) and observational work (e.g., Maiolino et al. 1995; Mouri & Taniguchi 2002; Buchanan et al. 2006; Deo et al. 2007; Meléndez et al. 2008b) that star formation is enhanced in obscured (i.e., type 2) AGNs. This would be inconsistent with the standard unified model (e.g., Antonucci 1993; Urry & Padovani 1995) where differences between obscured and unobscured AGNs are attributed to our viewing angle towards a central obscuring torus, and would suggest that the obscuring material in type 2 AGNs is related to star-formation activity in the host galaxy. However, we find that the distributions of nuclear SFRs, extended SFRs, total SFRs, and  $\text{SFR}/\text{BHAR}$  ratios for our sample do not exhibit any statistically significant differences between type 1 and type 2 Seyferts. While this result does not definitively rule out any difference between the star-forming properties of type 1 and type 2 AGNs, it does imply that such differences are not dramatic.

We note that results on star-formation activity as a function of Seyfert type likely depend on sample selection and the method used to measure the SFR. A comprehensive analysis of these factors is beyond the scope of this work, but their effect is apparent in previous published results. For example, Maiolino et al. (1995) studied a sample including 51 Seyferts from the CfA sample (Huchra & Burg 1992), 59 from the RSA sample, and 84 from the  $12 \mu\text{m}$  sample (Rush et al. 1993). By comparing ground-based  $10 \mu\text{m}$  observations with IRAS  $12\text{--}100 \mu\text{m}$  fluxes, they found that the extended IR emission in type 2 Seyferts tends to have a much redder color than that in type 1s, consistent with enhanced star formation in the type 2 galaxies. Similarly, Mouri & Taniguchi (2002) studied a sample of 50 RSA and 37 CfA Seyferts and found that Seyfert 2s had larger infrared/B-band and larger  $100 \mu\text{m}/60 \mu\text{m}$  flux ratios, implying that they were more often starburst or host-galaxy dominated. On the other hand, Imanishi & Wada (2004) studied a sample of 24 CfA and 33  $12 \mu\text{m}$  Seyferts and found no significant difference in  $3.3 \mu\text{m}$  aromatic feature luminosities between type 1 and type 2 Seyferts. More recently, Pereira-Santaella et al. (2010) found a significant enhancement in the fraction of type 2 Seyferts that exhibit excess [Ne III] emission associated with star formation for a heterogeneous sample of 201 Seyferts, but found no significant difference when considering more complete samples of 70 RSA and 97  $12 \mu\text{m}$  Seyferts.

## 7. CONCLUSIONS

We have measured BHARs based on the [O IV] emission line and nuclear, extended, and total SFRs based on the  $11.3 \mu\text{m}$  aromatic feature and extended  $24 \mu\text{m}$  continuum emission for a complete sample of Seyfert galaxies. We find a strong correlation between the nuclear star formation and black hole accretion, where the nuclear star formation is traced by the  $11.3 \mu\text{m}$  aromatic feature and  $24 \mu\text{m}$  emission external to the central PSF but within  $r = 1$  kpc (see Figures 5 and 9). On the other hand, the extended ( $r > 1$  kpc) and total SFRs are only weakly correlated with the BHAR (see Figure 10–12 and Table 2). This suggests a connection between gas on sub-kpc scales

that is forming stars and the gas on sub-pc scales that is accreting onto the black hole. While the physical processes that drive this relationship (e.g., mass loss from evolved stars, angular momentum loss from gravitational instabilities) are not clearly identified by these data, the connection is apparently unrelated to external processes on kpc scales in the host galaxy.

We thank the anonymous referee for helpful suggestions that have improved the paper. We acknowledge useful discussions with colleagues at all five Center for Galaxy Evolution campuses (UCI, UCLA, UCR, UCSB,

UCSD), where this work was presented prior to submission. We also acknowledge constructive feedback from David Ballantyne, Jill Bechtold, Xiaohui Fan, Alister Graham, Richard Green, Marcio Meléndez, John Moustakas, Greg Novak, Feryal Ozel, and Miguel Pereira-Santaella. AMD acknowledges support from the Southern California Center for Galaxy Evolution, a multi-campus research program funded by the University of California Office of Research. This work was also partially supported by contract 1255094 from Caltech/JPL to the University of Arizona.

*Facilities:* Spitzer

## REFERENCES

- Abramowicz, M. A., Czerny, B., Lasota, J. P., & Szuszkiewicz, E. 1988, *ApJ*, 332, 646
- Alexander, D. M., et al. 2003, *AJ*, 126, 539
- Antonucci, R. 1993, *ARA&A*, 31, 473
- Assef, R. J., et al. 2010, *ApJ*, 713, 970
- Atlee, D. W., Martini, P., Assef, R. J., Kelson, D. D., & Mulchaey, J. S. 2011, *ApJ*, 729, 22
- Ballantyne, D. R., Everett, J. E., & Murray, N. 2006, *ApJ*, 639, 740
- Ballantyne, D. R. 2008, *ApJ*, 685, 787
- Balmaverde, B., Baldi, R. D., & Capetti, A. 2008, *A&A*, 486, 119
- Barnes, J. E., & Hernquist, L. E. 1991, *ApJ*, 370, L65
- Bentz, M. C., et al. 2006, *ApJ*, 651, 775
- Bentz, M. C., et al. 2009, *ApJ*, 705, 199
- Bian, W., & Gu, Q. 2007, *ApJ*, 657, 159
- Bonfield, D. G., et al. 2011, *MNRAS*, arXiv:1103.3905
- Brand, K., et al. 2006, *ApJ*, 644, 143
- Brinchmann, J., Charlot, S., White, S. D. M., Tremonti, C., Kauffmann, G., Heckman, T., & Brinkmann, J. 2004, *MNRAS*, 351, 1151
- Buchanan, C. L., Gallimore, J. F., O’Dea, C. P., Baum, S. A., Axon, D. J., Robinson, A., Elitzur, M., & Elvis, M. 2006, *AJ*, 132, 401
- Calzetti, D., et al. 2007, *ApJ*, 666, 870
- Cappellari, M., Neumayer, N., Reunanen, J., van der Werf, P. P., de Zeeuw, P. T., & Rix, H.-W. 2009, *MNRAS*, 394, 660
- Cid Fernandes, R., Heckman, T., Schmitt, H., González Delgado, R. M., & Storch-Bergmann, T. 2001, *ApJ*, 558, 81
- Ciotti, L., & Ostriker, J. P. 2007, *ApJ*, 665, 1038
- Cisternas, M., et al. 2011, *ApJ*, 726, 57
- Cusumano, G., et al. 2010, *A&A*, 510, A48
- Davies, R. I., Sánchez, F. M., Genzel, R., Tacconi, L. J., Hicks, E. K. S., Friedrich, S., & Sternberg, A. 2007, *ApJ*, 671, 1388
- Denney, K. D., et al. 2006, *ApJ*, 653, 152
- Denney, K. D., et al. 2009, *ApJ*, 702, 1353
- Deo, R. P., Crenshaw, D. M., Kraemer, S. B., Dietrich, M., Elitzur, M., Teplitz, H., & Turner, T. J. 2007, *ApJ*, 671, 124
- Devereux, N., Ford, H., Tsvetanov, Z., & Jacoby, G. 2003, *AJ*, 125, 1226
- Diamond-Stanic, A. M., Rieke, G. H., & Rigby, J. R. 2009, *ApJ*, 698, 623
- Diamond-Stanic, A. M., & Rieke, G. H. 2010, *ApJ*, 724, 140
- Díaz-Santos, T., Alonso-Herrero, A., Colina, L., Packham, C., Levenson, N. A., Pereira-Santaella, M., Roche, P. F., & Telesco, C. M. 2010, *ApJ*, 711, 328
- Di Matteo, T., Springel, V., & Hernquist, L. 2005, *Nature*, 433, 604
- Dudík, R. P., Satyapal, S., Gliozzi, M., & Sambruna, R. M. 2005, *ApJ*, 620, 113
- Escala, A. 2007, *ApJ*, 671, 1264
- Ferrarese, L., & Merritt, D. 2000, *ApJ*, 539, L9
- Fu, H., et al. 2010, *ApJ*, 722, 653
- Gabor, J. M., et al. 2009, *ApJ*, 691, 705
- Gebhardt, K., et al. 2000, *ApJ*, 539, L13
- Genzel, R., et al. 1998, *ApJ*, 498, 579
- Graham, A. W. 2008, *ApJ*, 680, 143
- Graham, A. W., & Worley, C. C. 2008, *MNRAS*, 388, 1708
- Greene, J. E., et al. 2010, *ApJ*, 721, 26
- Grogin, N. A., et al. 2005, *ApJ*, 627, L97
- Groves, B., Dopita, M., & Sutherland, R. 2006, *A&A*, 458, 405
- Häring, N., & Rix, H.-W. 2004, *ApJ*, 604, L89
- Hatziminaoglou, E., et al. 2010, *A&A*, 518, L33
- Hao, C. N., Xia, X. Y., Mao, S., Wu, H., & Deng, Z. G. 2005, *ApJ*, 625, 78
- Hao, L., Jogee, S., Barazza, F. D., Marinova, I., & Shen, J. 2009, *Galaxy Evolution: Emerging Insights and Future Challenges*, 419, 402
- Heckman, T. M., Kauffmann, G., Brinchmann, J., Charlot, S., Tremonti, C., & White, S. D. M. 2004, *ApJ*, 613, 109
- Herrnstein, J. R., Moran, J. M., Greenhill, L. J., & Trotter, A. S. 2005, *ApJ*, 629, 719
- Ho, L. C., Filippenko, A. V., & Sargent, W. L. W. 1997, *ApJS*, 112, 315
- Ho, L. C., Filippenko, A. V., & Sargent, W. L. W. 1997, *ApJ*, 487, 591
- Ho, L. C., & Keto, E. 2007, *ApJ*, 658, 314
- Ho, L. C., Greene, J. E., Filippenko, A. V., & Sargent, W. L. W. 2009, *ApJS*, 183, 1
- Hobbs, A., Nayakshin, S., Power, C., & King, A. 2011, *MNRAS*, 413, 2633
- Hopkins, P. F., Hernquist, L., Cox, T. J., Di Matteo, T., Martini, P., Robertson, B., & Springel, V. 2005, *ApJ*, 630, 705
- Hopkins, P. F., & Hernquist, L. 2006b, *ApJS*, 166, 1
- Hopkins, P. F., & Quataert, E. 2010, *MNRAS*, 1085
- Houck, J. R., et al. 2004, *ApJS*, 154, 18
- Hu, J. 2008, *MNRAS*, 386, 2242
- Hunt, L. K., & Malkan, M. A. 1999, *ApJ*, 516, 660
- Huchra, J., & Burg, R. 1992, *ApJ*, 393, 90
- Imanishi, M., & Wada, K. 2004, *ApJ*, 617, 214
- Isobe, T., Feigelson, E. D., & Nelson, P. I. 1986, *ApJ*, 306, 490
- Jogee, S. 2006, *Physics of Active Galactic Nuclei at all Scales*, 693, 143
- Kauffmann, G., & Haehnelt, M. 2000, *MNRAS*, 311, 576
- Kauffmann, G., et al. 2003, *MNRAS*, 346, 1055
- Kawakatu, N., & Wada, K. 2008, *ApJ*, 681, 73
- Kelly, B. C. 2007, *ApJ*, 665, 1489
- Kennicutt, R. C., Jr. 1998, *ARA&A*, 36, 189
- Kennicutt, R. C., Jr. 1998, *ApJ*, 498, 541
- Kormendy, J. 1988, *ApJ*, 335, 40
- Kormendy, J., & Richstone, D. 1995, *ARA&A*, 33, 581
- Kormendy, J., Bender, R., & Cornell, M. E. 2011, *Nature*, 469, 374
- Laurikainen, E., Salo, H., & Buta, R. 2004, *ApJ*, 607, 103
- Lavalley, M., Isobe, T., & Feigelson, E. 1992, *Astronomical Data Analysis Software and Systems I*, 25, 245
- Lehmer, B. D., et al. 2005, *ApJS*, 161, 21
- Lutz, D., et al. 2008, *ApJ*, 684, 853
- Lutz, D., et al. 2010, *ApJ*, 712, 1287
- Maiolino, R., Ruiz, M., Rieke, G. H., & Keller, L. D. 1995, *ApJ*, 446, 561
- Maiolino, R., & Rieke, G. H. 1995, *ApJ*, 454, 95
- Magorrian, J., et al. 1998, *AJ*, 115, 2285
- Marconi, A., & Hunt, L. K. 2003, *ApJ*, 589, L21
- Meléndez, M., et al. 2008a, *ApJ*, 682, 94
- Meléndez, M., Kraemer, S. B., Schmitt, H. R., Crenshaw, D. M., Deo, R. P., Mushotzky, R. F., & Bruhweiler, F. C. 2008, *ApJ*, 689, 95
- Miller, J. M., Nowak, M., Markoff, S., Rupen, M. P., & Maitra, D. 2010, *ApJ*, 720, 1033
- Mouri, H., & Taniguchi, Y. 2002, *ApJ*, 565, 786
- Mulchaey, J. S., & Regan, M. W. 1997, *ApJ*, 482, L135
- Mullaney, J. R., Pannella, M., Daddi, E., et al. 2011, *MNRAS*, 1756, arXiv:1106.4284
- Narayan, R., & Yi, I. 1995, *ApJ*, 452, 710
- Netzer, H., et al. 2007, *ApJ*, 666, 806
- Netzer, H. 2009, *MNRAS*, 399, 1907
- Norman, C., & Scoville, N. 1988, *ApJ*, 332, 124
- O’Dowd, M. J., et al. 2009, *ApJ*, 705, 885
- Pierce, C. M., et al. 2007, *ApJ*, 660, L19
- Pilbratt, G. L., et al. 2010, *A&A*, 518, L1
- Peeters, E., Spoon, H. W. W., & Tielens, A. G. G. M. 2004, *ApJ*, 613, 986
- Peterson, B. M., et al. 2004, *ApJ*, 613, 682

- Pereira-Santaella, M., Diamond-Stanic, A. M., Alonso-Herrero, A., & Rieke, G. H. 2010, *ApJ*, 725, 2270
- Quataert, E., Di Matteo, T., Narayan, R., & Ho, L. C. 1999, *ApJ*, 525, L89
- Rieke, G. H., et al. 2004, *ApJS*, 154, 25
- Rieke, G. H., Alonso-Herrero, A., Weiner, B. J., Pérez-González, P. G., Blaylock, M., Donley, J. L., & Marcillac, D. 2009, *ApJ*, 692, 556
- Riffel, R., Pastoriza, M. G., Rodríguez-Ardila, A., & Bonatto, C. 2009, *MNRAS*, 400, 273
- Rigby, J. R., Diamond-Stanic, A. M., & Aniano, G. 2009, *ApJ*, 700, 1878
- Rush, B., Malkan, M. A., & Spinoglio, L. 1993, *ApJS*, 89, 1
- Sandage, A., & Tammann, G. A. 1987, *A Revised Shapley-Ames Catalog of Bright Galaxies* (2nd ed. Washington, DC: Carnegie Institution of Washington)
- Sanders, D. B., Soifer, B. T., Elias, J. H., Madore, B. F., Matthews, K., Neugebauer, G., & Scoville, N. Z. 1988, *ApJ*, 325, 74
- Satyapal, S., Dudik, R. P., O'Halloran, B., & Gliozzi, M. 2005, *ApJ*, 633, 86
- Serjeant, S., & Hatziminaoglou, E. 2009, *MNRAS*, 397, 265
- Schmidt, M. 1959, *ApJ*, 129, 243
- Schweitzer, M., et al. 2006, *ApJ*, 649, 79
- Scoville, N., et al. 2007, *ApJS*, 172, 1
- Shao, L., et al. 2010, *A&A*, 518, L26
- Shen, S., Mo, H. J., White, S. D. M., Blanton, M. R., Kauffmann, G., Voges, W., Brinkmann, J., & Csabai, I. 2003, *MNRAS*, 343, 978
- Shi, Y., et al. 2007, *ApJ*, 669, 841
- Shi, Y., Rieke, G. H., Ogle, P., Jiang, L., & Diamond-Stanic, A. M. 2009, *ApJ*, 703, 1107
- Shlosman, I., Begelman, M. C., & Frank, J. 1990, *Nature*, 345, 679
- Silverman, J. D., et al. 2009, *ApJ*, 696, 396
- Silk, J., & Rees, M. J. 1998, *A&A*, 331, L1
- Smith, J. D. T., et al. 2007, *ApJ*, 656, 770
- Smith, J. D. T., et al. 2007, *PASP*, 119, 1133
- Smith, H. A., Li, A., Li, M. P., et al. 2010, *ApJ*, 716, 490
- Somerville, R. S., Hopkins, P. F., Cox, T. J., Robertson, B. E., & Hernquist, L. 2008, *MNRAS*, 391, 481
- Storchi-Bergmann, T., González Delgado, R. M., Schmitt, H. R., Cid Fernandes, R., & Heckman, T. 2001, *ApJ*, 559, 147
- Sturm, E., Lutz, D., Verma, A., et al. 2002, *A&A*, 393, 821
- Thompson, T. A., Quataert, E., & Murray, N. 2005, *ApJ*, 630, 167
- Tielens, A. G. G. M. 2005, *The Physics and Chemistry of the Interstellar Medium* (Cambridge: Cambridge Univ. Press)
- Tommasin, S., Spinoglio, L., Malkan, M. A., & Fazio, G. 2010, *ApJ*, 709, 1257
- Tozzi, P., et al. 2006, *A&A*, 451, 457
- Tremaine, S., et al. 2002, *ApJ*, 574, 740
- Treyer, M., et al. 2010, *ApJ*, 719, 1191
- Urry, C. M., & Padovani, P. 1995, *PASP*, 107, 803
- Voit, G. M. 1992, *MNRAS*, 258, 841
- von Linden, S., Biermann, P. L., Duschl, W. J., Lesch, H., & Schmutzler, T. 1993, *A&A*, 280, 468
- Wada, K., & Norman, C. A. 2002, *ApJ*, 566, L21
- Wada, K. 2004, *Carnegie Observatories Astrophys. Ser. 1, Coevolution of Black Holes and Galaxies*, ed. L. C. Ho (Cambridge: Cambridge Univ. Press), 186
- Weaver, K. A., Meléndez, M., Mushotzky, R. F., et al. 2010, *ApJ*, 716, 1151
- Werner, M. W., et al. 2004, *ApJS*, 154, 1
- Wild, V., Kauffmann, G., Heckman, T., Charlot, S., Lemson, G., Brinchmann, J., Reichard, T., & Pasquali, A. 2007, *MNRAS*, 381, 543
- Wild, V., Heckman, T., & Charlot, S. 2010, *MNRAS*, 405, 933
- Wold, M., Lacy, M., Käuff, H. U., & Siebenmorgen, R. 2006, *A&A*, 460, 449
- Wu, Y., Charmandaris, V., Hao, L., Brandl, B. R., Bernard-Salas, J., Spoon, H. W. W., & Houck, J. R. 2006, *ApJ*, 639, 157
- Wyithe, J. S. B., & Loeb, A. 2003, *ApJ*, 595, 614

TABLE 1  
MEASUREMENTS AND DERIVED PARAMETERS

NAME (1)	11.3 $\mu\text{m}$ intensity, EW, SFR (2)	[Ne II] intensity, SFR (3)	aperture (4)	SFR $r = 1 \text{ kpc}$ (5)	SFR $r > 1 \text{ kpc}$ (6)	$\dot{M}_{BH}$ (7)	$M_{BH}$ value, method, ref. (8)	$L/L_{Edd}$ (9)
IC2560	$5.14 \pm 0.20 \times 10^{-7}$ , 0.10, $3.0 \times 10^{-1}$	$1.58 \pm 0.03 \times 10^{-7}$ , $9.7 \times 10^{-1}$	$0.71 \times 1.42$	$3.6 \times 10^{-1}$	$1.2 \times 10^0$	$5.1 \times 10^{-2}$	...	...
IC3639	$1.39 \pm 0.05 \times 10^{-6}$ , 0.20, $6.1 \times 10^{-1}$	$3.11 \pm 0.03 \times 10^{-7}$ , $1.4 \times 10^0$	$0.62 \times 1.23$	$7.0 \times 10^{-1}$	...	$1.1 \times 10^{-2}$	$6.8 \times 10^6$ , dis, 1	$7.2 \times 10^{-2}$
IRAS11215	$5.70 \pm 1.40 \times 10^{-8}$ , 0.02, $7.8 \times 10^{-2}$	$1.67 \pm 0.02 \times 10^{-8}$ , $2.4 \times 10^{-1}$	$1.09 \times 2.18$	$8.9 \times 10^{-2}$	...	$2.5 \times 10^{-2}$	...	...
MRK509	$6.50 \pm 0.14 \times 10^{-7}$ , 0.10, $4.7 \times 10^0$	$1.05 \pm 0.02 \times 10^{-7}$ , $8.0 \times 10^0$	$2.51 \times 5.02$	$4.7 \times 10^0$	...	$3.2 \times 10^{-1}$	$1.4 \times 10^8$ , rev, 2	$9.6 \times 10^{-2}$
NGC788	$1.17 \pm 0.15 \times 10^{-7}$ , 0.04, $1.2 \times 10^{-1}$	$5.16 \pm 0.17 \times 10^{-8}$ , $5.6 \times 10^{-1}$	$0.94 \times 1.89$	$1.2 \times 10^{-1}$	$2.1 \times 10^{-1}$	$3.6 \times 10^{-2}$	$3.2 \times 10^7$ , dis, 1	$4.8 \times 10^{-2}$
NGC1058	$1.91 \pm 0.06 \times 10^{-7}$ , 1.68, $5.7 \times 10^{-3}$	$8.94 \pm 1.10 \times 10^{-9}$ , $2.8 \times 10^{-3}$	$0.16 \times 0.32$	$2.1 \times 10^{-2}$	$5.9 \times 10^{-2}$	$< 2.3 \times 10^{-5}$	...	...
NGC1097	$1.50 \pm 0.03 \times 10^{-6}$ , 1.07, $1.4 \times 10^{-1}$	$1.44 \pm 0.03 \times 10^{-7}$ , $1.5 \times 10^{-1}$	$0.29 \times 0.58$	$2.3 \times 10^0$	$2.3 \times 10^0$	...	...	...
NGC1241	$5.83 \pm 1.01 \times 10^{-7}$ , 0.83, $5.9 \times 10^{-1}$	$7.88 \pm 0.57 \times 10^{-8}$ , $8.5 \times 10^{-1}$	$0.94 \times 1.88$	$5.9 \times 10^{-1}$	$2.4 \times 10^0$	$7.7 \times 10^{-3}$	$2.9 \times 10^7$ , dis, 1	$1.1 \times 10^{-2}$
NGC1275	$3.75 \pm 0.16 \times 10^{-7}$ , 0.03, $6.5 \times 10^{-1}$	$3.17 \pm 0.03 \times 10^{-7}$ , $5.8 \times 10^0$	$1.22 \times 2.45$	$6.5 \times 10^{-1}$	...	$2.6 \times 10^{-2}$	$3.8 \times 10^8$ , dis, 3	$2.9 \times 10^{-3}$
NGC1358	$8.07 \pm 1.81 \times 10^{-8}$ , 0.27, $8.2 \times 10^{-2}$	$2.79 \pm 0.31 \times 10^{-8}$ , $3.0 \times 10^{-1}$	$0.94 \times 1.87$	$8.2 \times 10^{-2}$	$1.2 \times 10^0$	$1.4 \times 10^{-2}$	$7.6 \times 10^7$ , dis, 1	$8.1 \times 10^{-3}$
NGC1365	$4.51 \pm 0.05 \times 10^{-6}$ , 0.34, $7.3 \times 10^{-1}$	$6.07 \pm 0.06 \times 10^{-7}$ , $1.0 \times 10^0$	$0.38 \times 0.75$	$4.8 \times 10^0$	$8.4 \times 10^0$	$3.8 \times 10^{-2}$	...	...
NGC1386	$9.73 \pm 0.34 \times 10^{-7}$ , 0.13, $3.8 \times 10^{-2}$	$1.18 \pm 0.04 \times 10^{-7}$ , $4.9 \times 10^{-2}$	$0.19 \times 0.37$	$5.4 \times 10^{-2}$	...	$6.0 \times 10^{-3}$	$1.7 \times 10^7$ , dis, 1	$1.5 \times 10^{-2}$
NGC1433	$6.08 \pm 0.15 \times 10^{-7}$ , 1.40, $3.8 \times 10^{-2}$	$4.96 \pm 0.21 \times 10^{-8}$ , $3.3 \times 10^{-2}$	$0.23 \times 0.46$	$6.9 \times 10^{-2}$	$1.7 \times 10^{-1}$	$< 6.7 \times 10^{-4}$	...	...
NGC1566	$1.06 \pm 0.01 \times 10^{-6}$ , 0.56, $1.4 \times 10^{-1}$	$7.46 \pm 0.20 \times 10^{-8}$ , $1.0 \times 10^{-1}$	$0.34 \times 0.68$	$1.8 \times 10^{-1}$	$2.5 \times 10^0$	$1.7 \times 10^{-3}$	...	...
NGC1667	$4.01 \pm 0.38 \times 10^{-7}$ , 1.16, $5.3 \times 10^{-1}$	$4.97 \pm 0.28 \times 10^{-8}$ , $6.9 \times 10^{-1}$	$1.07 \times 2.14$	$5.4 \times 10^{-1}$	$7.8 \times 10^0$	$1.3 \times 10^{-2}$	$7.6 \times 10^7$ , dis, 1	$7.3 \times 10^{-3}$
NGC2273	$2.69 \pm 0.03 \times 10^{-6}$ , 0.50, $7.6 \times 10^{-1}$	$3.20 \pm 0.03 \times 10^{-7}$ , $9.6 \times 10^{-1}$	$0.50 \times 0.99$	$7.6 \times 10^{-1}$	...	$6.2 \times 10^{-3}$	$2.0 \times 10^7$ , dis, 1	$1.3 \times 10^{-2}$
NGC2639	$1.34 \pm 0.05 \times 10^{-7}$ , 0.53, $8.6 \times 10^{-2}$	$7.55 \pm 0.09 \times 10^{-8}$ , $5.1 \times 10^{-1}$	$0.74 \times 1.49$	$1.0 \times 10^{-1}$	$1.2 \times 10^0$	$1.8 \times 10^{-3}$	$8.7 \times 10^7$ , dis, 3	$8.8 \times 10^{-4}$
NGC2655	$4.81 \pm 0.19 \times 10^{-7}$ , 0.47, $1.0 \times 10^{-1}$	$7.10 \pm 0.35 \times 10^{-8}$ , $1.6 \times 10^{-1}$	$0.43 \times 0.85$	$1.2 \times 10^{-1}$	$3.1 \times 10^{-1}$	$< 2.6 \times 10^{-3}$	$5.5 \times 10^7$ , dis, 3	$< 2.0 \times 10^{-3}$
NGC2685	$4.68 \pm 0.29 \times 10^{-8}$ , 0.24, $4.3 \times 10^{-3}$	$6.47 \pm 0.56 \times 10^{-9}$ , $6.3 \times 10^{-3}$	$0.28 \times 0.57$	$1.0 \times 10^{-2}$	$1.1 \times 10^{-1}$	$6.2 \times 10^{-5}$	$6.4 \times 10^6$ , dis, 3	$4.1 \times 10^{-4}$
NGC2992	$1.47 \pm 0.02 \times 10^{-6}$ , 0.28, $6.0 \times 10^{-1}$	$3.26 \pm 0.03 \times 10^{-7}$ , $1.4 \times 10^0$	$0.60 \times 1.19$	$7.7 \times 10^{-1}$	$5.4 \times 10^{-1}$	$8.4 \times 10^{-2}$	...	...
NGC3031	$2.54 \pm 0.16 \times 10^{-7}$ , 0.06, $1.2 \times 10^{-3}$	$1.79 \pm 0.03 \times 10^{-7}$ , $8.6 \times 10^{-3}$	$0.06 \times 0.13$	$1.7 \times 10^{-2}$	$1.7 \times 10^{-1}$	$3.2 \times 10^{-5}$	$8.0 \times 10^7$ , gas, 4	$1.7 \times 10^{-5}$
NGC3079	$2.12 \pm 0.03 \times 10^{-5}$ , 9.70, $3.1 \times 10^0$	$1.17 \pm 0.01 \times 10^{-6}$ , $1.8 \times 10^0$	$0.36 \times 0.71$	$3.4 \times 10^0$	$2.1 \times 10^0$	...	...	...
NGC3081	$3.66 \pm 0.12 \times 10^{-7}$ , 0.06, $1.5 \times 10^{-1}$	$9.60 \pm 0.10 \times 10^{-8}$ , $4.2 \times 10^{-1}$	$0.60 \times 1.19$	$1.5 \times 10^{-1}$	$3.1 \times 10^{-1}$	$7.6 \times 10^{-2}$	$2.3 \times 10^7$ , dis, 1	$1.4 \times 10^{-1}$
NGC3147	$2.13 \pm 0.19 \times 10^{-7}$ , 0.24, $1.3 \times 10^{-1}$	$3.10 \pm 0.30 \times 10^{-8}$ , $1.9 \times 10^{-1}$	$0.71 \times 1.43$	$1.5 \times 10^{-1}$	$4.7 \times 10^0$	$< 2.3 \times 10^{-3}$	$2.0 \times 10^8$ , dis, 3	$< 5.0 \times 10^{-4}$
NGC3185	$1.00 \pm 0.04 \times 10^{-6}$ , 1.60, $1.6 \times 10^{-1}$	$7.56 \pm 0.36 \times 10^{-8}$ , $1.3 \times 10^{-1}$	$0.37 \times 0.74$	$1.7 \times 10^{-1}$	$1.4 \times 10^{-1}$	$2.0 \times 10^{-3}$	$3.3 \times 10^6$ , dis, 3	$2.7 \times 10^{-2}$
NGC3227	$3.24 \pm 0.03 \times 10^{-6}$ , 0.46, $4.8 \times 10^{-1}$	$5.15 \pm 0.05 \times 10^{-7}$ , $8.1 \times 10^{-1}$	$0.36 \times 0.72$	$4.8 \times 10^{-1}$	$2.1 \times 10^{-1}$	$1.6 \times 10^{-2}$	$4.2 \times 10^7$ , rev, 5	$1.6 \times 10^{-2}$
NGC3254	$3.06 \pm 0.38 \times 10^{-8}$ , 0.46, $6.0 \times 10^{-3}$	$2.91 \pm 0.60 \times 10^{-9}$ , $6.0 \times 10^{-3}$	$0.41 \times 0.82$	$1.1 \times 10^{-2}$	$4.4 \times 10^{-1}$	$< 4.5 \times 10^{-4}$	$1.6 \times 10^7$ , dis, 3	$< 1.2 \times 10^{-3}$
NGC3281	$1.24 \pm 0.25 \times 10^{-6}$ , 0.10, $8.7 \times 10^{-1}$	$1.77 \pm 0.03 \times 10^{-7}$ , $1.3 \times 10^0$	$0.78 \times 1.56$	$8.7 \times 10^{-1}$	...	$1.9 \times 10^{-1}$	$1.9 \times 10^7$ , dis, 1	$4.2 \times 10^{-1}$
NGC3486	$8.82 \pm 1.70 \times 10^{-8}$ , 1.24, $1.7 \times 10^{-3}$	$5.83 \pm 3.20 \times 10^{-9}$ , $1.2 \times 10^{-3}$	$0.13 \times 0.26$	$2.8 \times 10^{-2}$	$7.0 \times 10^{-2}$	$< 9.9 \times 10^{-5}$	$1.5 \times 10^6$ , dis, 3	$< 2.9 \times 10^{-3}$
NGC3516	$2.29 \pm 0.26 \times 10^{-7}$ , 0.04, $1.2 \times 10^{-1}$	$4.54 \pm 0.39 \times 10^{-8}$ , $2.5 \times 10^{-1}$	$0.68 \times 1.36$	$2.0 \times 10^{-1}$	...	$3.7 \times 10^{-2}$	$4.3 \times 10^7$ , rev, 2	$3.7 \times 10^{-2}$
NGC3735	$7.59 \pm 0.30 \times 10^{-7}$ , 0.31, $4.5 \times 10^{-1}$	$5.84 \pm 0.37 \times 10^{-8}$ , $3.6 \times 10^{-1}$	$0.72 \times 1.43$	$5.1 \times 10^{-1}$	$2.9 \times 10^0$	$3.4 \times 10^{-2}$	$3.3 \times 10^7$ , dis, 3	$4.5 \times 10^{-2}$
NGC3783	$1.10 \pm 0.20 \times 10^{-7}$ , 0.01, $5.0 \times 10^{-2}$	$1.44 \pm 0.21 \times 10^{-7}$ , $7.0 \times 10^{-1}$	$0.63 \times 1.26$	$5.0 \times 10^{-2}$	...	$2.9 \times 10^{-2}$	$3.0 \times 10^7$ , rev, 2	$4.1 \times 10^{-2}$
NGC3941	$1.29 \pm 0.35 \times 10^{-8}$ , 0.05, $1.6 \times 10^{-3}$	$6.25 \pm 0.61 \times 10^{-9}$ , $8.3 \times 10^{-3}$	$0.33 \times 0.66$	$1.0 \times 10^{-2}$	$1.5 \times 10^{-1}$	$< 1.8 \times 10^{-4}$	$2.6 \times 10^7$ , dis, 3	$< 3.0 \times 10^{-4}$
NGC3976	$1.50 \pm 0.25 \times 10^{-7}$ , 0.71, $7.5 \times 10^{-2}$	$1.34 \pm 0.30 \times 10^{-8}$ , $7.1 \times 10^{-2}$	$0.66 \times 1.32$	$9.3 \times 10^{-2}$	$1.7 \times 10^0$	$5.7 \times 10^{-4}$	$1.1 \times 10^8$ , dis, 3	$2.2 \times 10^{-4}$
NGC3982	$3.21 \pm 0.19 \times 10^{-7}$ , 0.67, $3.3 \times 10^{-2}$	$5.59 \pm 0.27 \times 10^{-8}$ , $6.0 \times 10^{-2}$	$0.30 \times 0.59$	$1.5 \times 10^{-1}$	$4.9 \times 10^{-1}$	$7.3 \times 10^{-4}$	$1.2 \times 10^6$ , dis, 1	$2.5 \times 10^{-2}$
NGC4051	$1.12 \pm 0.03 \times 10^{-6}$ , 0.12, $1.1 \times 10^{-1}$	$1.04 \pm 0.06 \times 10^{-7}$ , $1.1 \times 10^{-1}$	$0.30 \times 0.59$	$1.3 \times 10^{-1}$	$8.8 \times 10^{-1}$	$5.0 \times 10^{-3}$	$1.7 \times 10^6$ , rev, 5	$1.2 \times 10^{-1}$
NGC4138	$1.05 \pm 0.03 \times 10^{-7}$ , 0.18, $1.1 \times 10^{-2}$	$1.71 \pm 0.05 \times 10^{-8}$ , $1.8 \times 10^{-2}$	$0.30 \times 0.59$	$2.8 \times 10^{-2}$	$1.1 \times 10^{-1}$	$3.2 \times 10^{-4}$	$1.8 \times 10^7$ , dis, 3	$7.7 \times 10^{-4}$
NGC4151	$4.03 \pm 1.72 \times 10^{-7}$ , 0.02, $5.8 \times 10^{-2}$	$2.46 \pm 0.07 \times 10^{-7}$ , $3.8 \times 10^{-1}$	$0.35 \times 0.71$	$5.8 \times 10^{-2}$	...	$5.5 \times 10^{-2}$	$4.6 \times 10^7$ , rev, 6	$5.2 \times 10^{-2}$
NGC4235	$1.24 \pm 0.15 \times 10^{-7}$ , 0.16, $5.4 \times 10^{-2}$	$2.99 \pm 0.29 \times 10^{-8}$ , $1.4 \times 10^{-1}$	$0.61 \times 1.23$	$6.5 \times 10^{-2}$	$1.4 \times 10^{-1}$	$2.2 \times 10^{-3}$	$4.4 \times 10^7$ , dis, 3	$2.2 \times 10^{-3}$
NGC4258	$3.40 \pm 0.03 \times 10^{-7}$ , 0.15, $7.7 \times 10^{-3}$	$7.47 \pm 0.07 \times 10^{-8}$ , $1.8 \times 10^{-2}$	$0.14 \times 0.28$	$4.6 \times 10^{-2}$	$3.9 \times 10^{-1}$	$2.6 \times 10^{-4}$	$3.8 \times 10^7$ , mas, 7	$3.0 \times 10^{-4}$
NGC4378	$1.29 \pm 0.04 \times 10^{-7}$ , 0.62, $5.6 \times 10^{-2}$	$5.96 \pm 0.73 \times 10^{-9}$ , $2.7 \times 10^{-2}$	$0.61 \times 1.23$	$5.9 \times 10^{-2}$	$5.6 \times 10^{-1}$	$< 1.2 \times 10^{-3}$	$1.1 \times 10^8$ , dis, 3	$< 4.6 \times 10^{-4}$
NGC4388	$1.58 \pm 0.03 \times 10^{-6}$ , 0.23, $1.6 \times 10^{-1}$	$4.98 \pm 0.05 \times 10^{-7}$ , $5.2 \times 10^{-1}$	$0.29 \times 0.59$	$2.1 \times 10^{-1}$	$2.4 \times 10^{-1}$	$4.8 \times 10^{-2}$	$1.7 \times 10^7$ , dis, 1	$1.2 \times 10^{-1}$
NGC4395	$2.82 \pm 0.31 \times 10^{-8}$ , 0.18, $2.1 \times 10^{-4}$	$2.64 \pm 0.04 \times 10^{-8}$ , $2.1 \times 10^{-3}$	$0.08 \times 0.16$	$1.3 \times 10^{-3}$	$2.0 \times 10^{-2}$	$8.1 \times 10^{-5}$	$3.6 \times 10^5$ , rev, 2	$9.6 \times 10^{-3}$
NGC4477	$1.55 \pm 0.04 \times 10^{-7}$ , 0.62, $1.5 \times 10^{-2}$	$1.96 \pm 0.07 \times 10^{-8}$ , $2.0 \times 10^{-2}$	$0.29 \times 0.59$	$2.2 \times 10^{-2}$	$2.5 \times 10^{-2}$	$2.0 \times 10^{-4}$	$8.2 \times 10^7$ , dis, 3	$1.0 \times 10^{-4}$
NGC4501	$3.06 \pm 0.03 \times 10^{-7}$ , 0.87, $3.0 \times 10^{-2}$	$3.94 \pm 0.05 \times 10^{-8}$ , $4.1 \times 10^{-2}$	$0.29 \times 0.59$	$6.8 \times 10^{-2}$	$1.7 \times 10^0$	$4.0 \times 10^{-4}$	$7.2 \times 10^7$ , dis, 1	$2.3 \times 10^{-4}$
NGC4507	$7.95 \pm 0.18 \times 10^{-7}$ , 0.06, $9.9 \times 10^{-1}$	$2.81 \pm 0.03 \times 10^{-7}$ , $3.7 \times 10^0$	$1.04 \times 2.08$	$9.9 \times 10^{-1}$	...	$6.7 \times 10^{-2}$	$3.8 \times 10^7$ , dis, 1	$7.5 \times 10^{-2}$
NGC4565	$1.47 \pm 0.19 \times 10^{-7}$ , 0.37, $4.9 \times 10^{-3}$	$1.99 \pm 0.29 \times 10^{-8}$ , $6.9 \times 10^{-3}$	$0.17 \times 0.34$	$4.0 \times 10^{-2}$	$5.3 \times 10^{-1}$	$2.1 \times 10^{-4}$	$2.9 \times 10^7$ , dis, 3	$3.2 \times 10^{-4}$
NGC4579	$3.13 \pm 0.13 \times 10^{-7}$ , 0.26, $3.1 \times 10^{-2}$	$1.03 \pm 0.02 \times 10^{-7}$ , $1.1 \times 10^{-1}$	$0.29 \times 0.59$	$4.7 \times 10^{-2}$	$4.7 \times 10^{-1}$	...	...	...
NGC4593	$2.65 \pm 0.29 \times 10^{-7}$ , 0.04, $1.6 \times 10^{-1}$	$4.02 \pm 0.38 \times 10^{-8}$ , $2.5 \times 10^{-1}$	$0.72 \times 1.44$	$1.6 \times 10^{-1}$	$4.8 \times 10^{-1}$	$1.3 \times 10^{-2}$	$9.8 \times 10^6$ , rev, 8	$5.5 \times 10^{-2}$
NGC4594	$3.77 \pm 1.09 \times 10^{-8}$ , 0.06, $5.3 \times 10^{-3}$	$6.63 \pm 0.07 \times 10^{-8}$ , $9.8 \times 10^{-2}$	$0.35 \times 0.70$	$3.4 \times 10^{-2}$	$6.6 \times 10^{-1}$	$5.3 \times 10^{-4}$	$5.7 \times 10^8$ , sta, 10	$4.0 \times 10^{-5}$
NGC4639	$1.67 \pm 0.03 \times 10^{-7}$ , 0.67, $1.7 \times 10^{-2}$	$9.46 \pm 0.57 \times 10^{-9}$ , $9.9 \times 10^{-3}$	$0.29 \times 0.59$	$2.1 \times 10^{-2}$	$1.2 \times 10^{-1}$	$< 1.9 \times 10^{-4}$	$7.1 \times 10^6$ , dis, 3	$< 1.1 \times 10^{-3}$
NGC4698	$9.75 \pm 3.34 \times 10^{-9}$ , 0.08, $9.7 \times 10^{-4}$	$5.85 \pm 0.50 \times 10^{-9}$ , $6.1 \times 10^{-3}$	$0.29 \times 0.59$	$5.1 \times 10^{-3}$	$7.4 \times 10^{-2}$	$< 3.1 \times 10^{-4}$	$4.1 \times 10^7$ , dis, 3	$< 3.3 \times 10^{-4}$
NGC4725	$2.83 \pm 1.68 \times 10^{-8}$ , 0.06, $1.5 \times 10^{-3}$	$6.01 \pm 2.35 \times 10^{-9}$ , $3.4 \times 10^{-3}$	$0.22 \times 0.43$	$1.0 \times 10^{-2}$	$3.4 \times 10^{-1}$	$1.5 \times 10^{-4}$	$3.2 \times 10^7$ , dis, 3	$2.0 \times 10^{-4}$
NGC4939	$7.78 \pm 0.94 \times 10^{-8}$ , 0.07, $5.9 \times 10^{-2}$	$6.05 \pm 0.16 \times 10^{-8}$ , $4.9 \times 10^{-1}$	$0.81 \times 1.63$	$5.9 \times 10^{-2}$	$2.4 \times 10^0$	$7.7 \times 10^{-2}$	...	...

TABLE 1 — *Continued*

NAME (1)	11.3 $\mu\text{m}$ intensity, EW, SFR (2)	[Ne II] intensity, SFR (3)	aperture (4)	SFR $r = 1$ kpc (5)	SFR $r > 1$ kpc (6)	$\dot{M}_{BH}$ (7)	$M_{BH}$ value, method, ref. (8)	$L/L_{Edd}$ (9)
NGC4941	1.31 $\pm$ 0.09e−07, 0.08, 1.3e−02	1.09 $\pm$ 0.01e−07, 1.1e−01	0.29 $\times$ 0.59	1.3e−02	1.2e−01	4.1e−03	3.4e+06, dis, 1	5.2e−02
NGC4945	2.36 $\pm$ 0.02e−05, 26.11, 1.5e−01	5.47 $\pm$ 0.05e−06, 3.7e−01	0.08 $\times$ 0.15	5.6e−01	1.1e+00	...	...	...
NGC5005	3.37 $\pm$ 0.05e−06, 2.59, 5.4e−01	3.27 $\pm$ 0.04e−07, 5.5e−01	0.37 $\times$ 0.74	6.3e−01	1.8e+00	...	...	...
NGC5033	1.23 $\pm$ 0.02e−06, 1.32, 1.5e−01	1.27 $\pm$ 0.02e−07, 1.6e−01	0.33 $\times$ 0.65	3.3e−01	1.8e+00	1.8e−03	4.4e+07, dis, 1	1.7e−03
NGC5128	2.80 $\pm$ 0.28e−06, 0.06, 1.8e−02	2.08 $\pm$ 0.02e−06, 1.4e−01	0.08 $\times$ 0.15	3.7e−01	7.1e−01	1.4e−03	7.0e+07, sta, 10	8.4e−04
NGC5135	4.93 $\pm$ 0.05e−06, 1.05, 5.8e+00	8.13 $\pm$ 0.08e−07, 1.0e+01	1.01 $\times$ 2.01	6.1e+00	3.6e+00	1.3e−01	2.2e+07, dis, 1	2.5e−01
NGC5194	6.80 $\pm$ 0.15e−07, 0.88, 1.7e−02	1.68 $\pm$ 0.02e−07, 4.4e−02	0.15 $\times$ 0.29	2.8e−01	2.2e+00	7.4e−04	8.9e+06, dis, 1	3.5e−03
NGC5273	3.20 $\pm$ 0.19e−07, 0.63, 5.1e−02	2.74 $\pm$ 0.30e−08, 4.6e−02	0.37 $\times$ 0.74	5.7e−02	...	1.2e−03	2.1e+06, dis, 1	2.5e−02
NGC5395	1.22 $\pm$ 0.05e−07, 1.30, 9.4e−02	4.44 $\pm$ 0.50e−09, 3.6e−02	0.82 $\times$ 1.63	9.9e−02	2.4e+00	...	...	...
NGC5427	2.69 $\pm$ 0.04e−07, 0.38, 1.5e−01	4.03 $\pm$ 0.06e−08, 2.4e−01	0.71 $\times$ 1.41	2.3e−01	2.9e+00	3.7e−03	...	...
NGC5506	1.82 $\pm$ 0.06e−06, 0.10, 5.8e−01	5.60 $\pm$ 0.06e−07, 1.9e+00	0.52 $\times$ 1.05	5.8e−01	...	1.2e−01	4.5e+06, dis, 1	1.1e+00
NGC5631	2.61 $\pm$ 0.38e−08, 0.20, 9.8e−03	4.41 $\pm$ 0.55e−09, 1.7e−02	0.57 $\times$ 1.14	1.3e−02	3.1e−02	< 8.6e−04	6.7e+07, dis, 3	< 5.5e−04
NGC5643	1.98 $\pm$ 0.09e−06, 0.40, 1.4e−01	2.29 $\pm$ 0.09e−07, 1.8e−01	0.25 $\times$ 0.50	2.4e−01	8.7e−01	1.4e−02	...	...
NGC5728	2.10 $\pm$ 0.02e−06, 1.44, 1.2e+00	2.18 $\pm$ 0.02e−07, 1.4e+00	0.72 $\times$ 1.43	1.4e+00	1.7e+00	1.1e−01	1.6e+08, dis, 1	2.8e−02
NGC5899	6.42 $\pm$ 0.32e−07, 0.92, 4.1e−01	8.93 $\pm$ 0.35e−08, 6.1e−01	0.75 $\times$ 1.49	4.3e−01	2.4e+00	2.2e−02	...	...
NGC6221	6.50 $\pm$ 0.07e−06, 0.83, 8.5e−01	1.77 $\pm$ 0.02e−06, 2.4e+00	0.34 $\times$ 0.67	1.7e+00	3.6e+00	...	...	...
NGC6300	3.07 $\pm$ 0.03e−06, 0.34, 2.1e−01	1.76 $\pm$ 0.02e−07, 1.3e−01	0.24 $\times$ 0.49	2.1e−01	9.3e−01	3.4e−03	...	...
NGC6814	2.33 $\pm$ 0.21e−07, 0.10, 5.4e−02	6.15 $\pm$ 0.36e−08, 1.5e−01	0.45 $\times$ 0.89	9.2e−02	1.4e+00	9.7e−03	1.8e+07, rev, 11	2.2e−02
NGC6951	2.03 $\pm$ 0.06e−06, 1.59, 4.1e−01	2.44 $\pm$ 0.04e−07, 5.3e−01	0.42 $\times$ 0.84	8.7e−01	2.0e+00	2.6e−03	2.2e+07, dis, 3	5.0e−03
NGC7130	2.61 $\pm$ 0.07e−06, 0.62, 4.3e+00	5.29 $\pm$ 0.08e−07, 9.3e+00	1.20 $\times$ 2.40	4.3e+00	6.7e+00	3.9e−02	3.3e+07, dis, 1	5.0e−02
NGC7172	1.46 $\pm$ 0.06e−06, 1.70, 7.3e−01	2.22 $\pm$ 0.02e−07, 1.2e+00	0.66 $\times$ 1.31	7.9e−01	6.8e−01	3.1e−02	4.7e+07, dis, 1	2.8e−02
NGC7213	2.04 $\pm$ 0.03e−07, 0.06, 4.4e−02	1.34 $\pm$ 0.03e−07, 3.1e−01	0.43 $\times$ 0.87	4.4e−02	3.9e−01	...	...	...
NGC7314	2.55 $\pm$ 0.11e−07, 0.12, 3.9e−02	6.40 $\pm$ 0.14e−08, 1.0e−01	0.36 $\times$ 0.73	6.6e−02	6.2e−01	1.6e−02	...	...
NGC7410	1.74 $\pm$ 0.13e−07, 1.17, 3.8e−02	2.91 $\pm$ 0.19e−08, 6.6e−02	0.43 $\times$ 0.87	4.6e−02	3.0e−01	< 4.1e−03	...	...
NGC7469	5.40 $\pm$ 0.05e−06, 0.38, 8.5e+00	1.17 $\pm$ 0.01e−06, 1.9e+01	1.17 $\times$ 2.34	8.5e+00	...	...	1.2e+07, rev, 5	...
NGC7479	8.70 $\pm$ 2.20e−07, 0.14, 3.2e−01	1.16 $\pm$ 0.11e−07, 4.5e−01	0.57 $\times$ 1.13	3.2e−01	1.7e+00	2.8e−03	4.8e+07, dis, 3	2.5e−03
NGC7496	1.42 $\pm$ 0.03e−06, 0.49, 2.7e−01	2.77 $\pm$ 0.04e−07, 5.5e−01	0.40 $\times$ 0.81	2.7e−01	5.1e−01	...	...	...
NGC7582	4.10 $\pm$ 0.04e−06, 1.42, 7.0e−01	3.60 $\pm$ 0.04e−07, 6.5e−01	0.38 $\times$ 0.77	2.1e+00	1.9e+00	5.8e−02	5.5e+07, gas, 12	4.5e−02
NGC7590	4.57 $\pm$ 0.81e−07, 1.54, 7.8e−02	2.73 $\pm$ 0.34e−08, 4.9e−02	0.38 $\times$ 0.77	1.6e−01	1.1e+00	8.1e−04	6.2e+06, dis, 1	5.6e−03
NGC7743	3.42 $\pm$ 0.03e−07, 1.23, 7.2e−02	4.52 $\pm$ 0.28e−08, 1.0e−01	0.43 $\times$ 0.85	7.9e−02	4.9e−02	9.4e−04	5.3e+06, dis, 3	7.6e−03

NOTE. — Col. (1): Galaxy name. Col. (2): 11.3  $\mu\text{m}$  aromatic feature intensity [ $\text{W m}^{-2} \text{sr}^{-1}$ ], equivalent width [ $\mu\text{m}$ ], and derived star-formation rate [ $\text{M}_{\odot} \text{yr}^{-1}$ ]. Col. (3): [Ne II] intensity [ $\text{W m}^{-2} \text{sr}^{-1}$ ] and derived star-formation rate [ $\text{M}_{\odot} \text{yr}^{-1}$ ]. Col. (4): Physical size of the  $3.6'' \times 7.2''$  aperture used for the two previous columns [kpc $\times$ kpc]. Col. (5): Star-formation rate inside  $r = 1$  kpc [ $\text{M}_{\odot} \text{yr}^{-1}$ ]. Col. (6): Star-formation rate outside  $r = 1$  kpc [ $\text{M}_{\odot} \text{yr}^{-1}$ ]. Col. (7): Black hole accretion rate derived from the [O IV] luminosity [ $\text{M}_{\odot} \text{yr}^{-1}$ ]. Col. (8): Black hole mass [ $\text{M}_{\odot}$ ], method used to determine black hole mass (mas: maser dynamics, dis: bulge velocity dispersion, rev: reverberation mapping, gas: gas dynamics, ste: stellar dynamics), and reference for black hole mass (see below). Col. (9): Eddington ratio. References: (1) Bian & Gu (2007). (2) Peterson et al. (2004). (3) Ho et al. (2009). (4) Devereux et al. (2003). (5) Denney et al. (2009). (6) Bentz et al. (2006). (7) Herrnstein et al. (2005). (8) Denney et al. (2006). (9) Kormendy (1988). (10) Cappellari et al. (2009). (11) Bentz et al. (2009). (12) Wold et al. (2006).



TABLE 2  
CORRELATION ANALYSIS: SFR v.  $\dot{M}_{BH}$

aperture radius	11.3 $\mu\text{m}$ PAH	24 $\mu\text{m}$ continuum	$\alpha$	$\beta$	$\sigma$	luminosity correlation	flux correlation	flux probability
<300 pc>	Y	N	$0.88^{+0.36}_{-0.31}$	$0.80^{+0.14}_{-0.12}$	$0.37^{+0.18}_{-0.20}$	$0.95^{+0.04}_{-0.07}$	$0.69^{+0.11}_{-0.13}$	$< 1 \times 10^{-6}$
1 kpc	Y	Y	$0.67^{+0.39}_{-0.29}$	$0.61^{+0.15}_{-0.11}$	$0.41^{+0.23}_{-0.24}$	$0.93^{+0.06}_{-0.10}$	$0.49^{+0.16}_{-0.18}$	$2.9 \times 10^{-5}$
> 1 kpc	N	Y	$1.30^{+0.76}_{-0.45}$	$0.57^{+0.28}_{-0.17}$	$0.73^{+0.13}_{-0.20}$	$0.78^{+0.13}_{-0.20}$	$0.33^{+0.21}_{-0.22}$	0.02
$r_{galaxy}$	Y	Y	$1.59^{+1.15}_{-0.57}$	$0.71^{+0.45}_{-0.22}$	$0.86^{+0.22}_{-0.20}$	$0.65^{+0.17}_{-0.22}$	$0.14^{+0.20}_{-0.21}$	0.39

NOTE. — The quoted values in columns 4–8 correspond to the median of the posterior distribution, and the range that encompasses 90% of that distribution (see Kelly 2007). The values in the last column correspond to the probability that no correlation exists in the flux-flux version of the relationship, based on generalized Spearman's  $\rho$  (Isobe et al. 1986; Lavalley et al. 1992).